Establishing sample-preparation protocols for X-ray phase-contrast CT of rodent spinal cords: aldehyde fixations and osmium impregnation

Giacomo E. Barbone (Investigation) (Methodology) (Software) (Validation) (Formal analysis) (Data curation) (Visualization) (Writing - original draft), Alberto Bravin (Conceptualization) (Methodology) (Resources) (Writing - review and editing) (Supervision), Alberto Mittone (Investigation) (Methodology) (Software) (Validation) (Data curation) (Writing - review and editing), Markus J. Kraiger (Investigation) (Validation) (Data curation), Martin Hrabě de Angelis (Resources) (Supervision) (Funding acquisition), Mario Bossi (Investigation) (Data curation), Elisa Ballarini (Investigation) (Validation) (Writing - review and editing), Virginia Rodriguez-Menendez (Investigation) (Validation) (Writing - review and editing), Cecilia Ceresa (Investigation) (Data curation), Guido Cavaletti (Conceptualization) (Resources) (Writing - review and editing) (Supervision) (Funding acquisition), Paola Coan (Conceptualization) (Methodology) (Writing - review and editing) (Supervision) (Funding acquisition) (Project administration)

PII: S0165-0270(20)30167-9
DOI: https://doi.org/10.1016/j.jneumeth.2020.108744
Reference: NSM 108744

To appear in: *Journal of Neuroscience Methods*

Received Date: 10 March 2020
Revised Date: 14 April 2020
Accepted Date: 15 April 2020

Please cite this article as: { doi: https://doi.org/

Establishing sample-preparation protocols for X-ray phase-contrast CT of rodent spinal cords: aldehyde fixations and osmium impregnation.

Authors:
Giacomo E. Barbone (1), MSc., Mr., giacomo.e.barbone@gmail.com, **Alberto Bravin** (2), PhD, Dr., bravin@esrf.fr, **Alberto Mittone** (2#), PhD, Dr., amittone@cells.es, **Markus J. Kraiger** (3), PhD, Dr., markus.kraiger@helmholtz-muenchen.de, **Martin Hrabě de Angelis** (3,4,5), PhD, Prof. Dr., hrabe@helmholtz-muenchen.de, **Mario Bossi** (6,7), Mr., mario.bossi@unimib.it, **Elisa Ballarini** (6,7), PhD, Dr., elisa.ballarini@unimib.it, **Virginia Rodriguez-Menendez** (6,7), PhD, Dr., virginia.rodriguez1@unimib.it, **Cecilia Ceresa** (6,7), PhD, Dr., cecilia.ceresa@gmail.com, **Guido Cavaletti** (6,7), MD, Prof. Dr., guido.cavaletti@unimib.it, **Paola Coan *** (1,8) PhD, Prof. Dr., paola.coan@physik.uni-muenchen.de

(1) Department of Medical Physics, Faculty of Physics, Ludwig-Maximilians-Universität München, Garching, Germany.
(2) European Synchrotron Radiation Facility, Grenoble, France.
(#) Present address: CELLS-ALBA Synchrotron, Cerdanyola del Vallès, Spain.
(3) Institute of Experimental Genetics and German Mouse Clinic, German Research Center for Environmental Health, Neuherberg, Germany;
(4) Department of Experimental Genetics, School of Life Science Weihenstephan, Technical University of Munich, Freising, Germany.
(5) German Center for Diabetes Research, Neuherberg, Germany.
(6) Experimental Neurology Unit, School of Medicine and Surgery, University of Milano-Bicocca, Monza, Italy.
(7) Milan Center for Neuroscience, University of Milano-Bicocca, Milan, Italy.
(8) Department of Clinical Radiology, Faculty of Medicine, Ludwig-Maximilians-Universität München, Munich, Germany.

***Corresponding Author:**
Prof. Dr. Paola Coan
paola.coan@physik.uni-muenchen.de
Phone: +49(0)89 289-14062
Fax: +49-(89)-289-14072
Department of Medical Physics, Faculty of Physics, Ludwig-Maximilians-Universität München,
Am Coulombwall 1, D-85748 Garching

Highlights:

- X-ray phase-contrast CT (X-PCI-CT) enables label-free 3D nervous-tissue microscopy
- Multiscale X-PCI-CT captures full-organ to intra-cellular spinal cord neuroanatomy
- Combination of aldehyde fixatives optimizes visualizations of deep micro-vasculature
- Osmium impregnation highlights white-matter and individual motor neuron perikarya
- *Post-mortem* X-PCI-CT resolving power can exceed that of *post-mortem* high-field MRI

Abstract:

Background: Dense and unbiased cellular-resolution representations of extended volumetric central nervous system soft-tissue anatomy are difficult to obtain, even in experimental *post-mortem* settings. Interestingly, X-ray phase-contrast computed tomography (X-PCI-CT), an emerging soft-tissue-sensitive volumetric imaging technique, can provide multiscale organ- to cellular-level morphological visualizations of neuroanatomical structure.

New Method: Here, we tested different nervous-tissue fixation procedures, conventionally used for transmission electron microscopy, to better establish X-PCI-CT-specific sample-preparation protocols. Extracted rat spinal medullas were alternatively fixed with a standard paraformaldehyde-only aldehyde-based protocol, or in combination with glutaraldehyde. Some specimens were additionally post-fixed with osmium tetroxide. Multiscale X-PCI-CT datasets were collected at several synchrotron radiation facilities, using state-of-the-art setups with effective image voxel sizes of 3.0^3 to 0.3^3 μm^3, and compared to high-field magnetic resonance imaging, histology and vascular fluorescence microscopy data.

Results: Multiscale X-PCI-CT of aldehyde-fixed spinal cord specimens resulted in dense histology-like volumetric representations and quantifications of extended deep spinal micro-vascular networks and of intra-medullary cell populations. Osmium post-fixation increased intra-medullary contrast between white and gray-matter tissues, and enhanced delineation of intra-medullary cellular structure, e.g. axon fibers and motor neuron perikarya.

Comparison with Existing Methods: Volumetric X-PCI-CT provides complementary contrast and higher spatial resolution compared to 9.4 T MRI. X-PCI-CT's advantage over planar histology is the volumetric nature of the cellular-level data obtained, using samples much larger than those fit for volumetric vascular fluorescence microscopy.

Conclusions: Deliberately choosing (post-)fixation protocols tailored for optimal nervous-tissue structural preservation is of paramount importance in achieving effective and targeted neuroimaging via the X-PCI-CT technique.

Keywords:

Micro-CT, X-ray phase-contrast, Synchrotron radiation, Multiscale neuroimaging, Spinal cord imaging, Soft-tissue fixation.

1. Introduction:

The diagnosis and study of spinal vascular diseases, such as hemorrhage and vasculitis, and of complex neurodegenerative disorders involving the spinal cord, such as amyotrophic lateral sclerosis (ALS) or multiple sclerosis (MS), require first of all the localization of small pathological lesions within the extended anatomy of the central nervous system (CNS), followed by the detailed examination of microstructural and even molecular content within identified pathological tissues. Up to now, though, a non-destructive 3D technique for the multiscale investigation of CNS tissue anatomy and pathology, i.e. which can provide both organ-level and cellular-level 3D structural information, is still not available amongst cutting-edge neuroimaging techniques, both in clinical and research settings. Histological methods at the technological forefront of cellular-level structural and functional interrogations, for example, are still limited by an intrinsically 2D analysis of thin planar tissue sections and by labor-intensive protocols, lasting up to tens of hours when the goal is a 3D reconstruction[1]. Even the whole human brain histological atlases achievable today[2], with in-plane cellular-resolution approaching 1µm/pixel, come short of a fully-volumetric CNS network representation. First, the resolution of the third dimension is restricted by the slice thickness, which determines a minimal sampling interval usually of around 50 µm. Second, alleged 3D histological datasets need to face the error-prone challenge of slice-to-slice alignment, and, last, the projection of volumetric tissue structures within an individual histological slice onto a 2D plane leads to at least some degree of stereological bias[3] of histology-based neuro-morphological quantifications. Besides, tissue sectioning is notoriously sample-invasive and frequently causes tissue disruption and artifact formation in tissue sections, including both larger cracks as well as smaller tears in white and gray matter alike. Last, despite their undisputed and invaluable role in neuroscience, histological techniques rely heavily on staining and labeling of tissues to derive structural contrast and functional information, and thus fail to deliver a completely direct and dense characterization of CNS structure. Electron microscopy (EM) technology, for its part, enables unprecedented visualizations of even ultra-structural nervous tissue components, e.g. brain neuropil or spinal cord axonal microstructure[4], and arguably affords the densest and most detailed representations of nervous tissue morphology available today. EM too, though, normally involves osmium staining, and is limited by tissue-sectioning procedures even more challenging than those required for histology.

The leading non-destructive 3D neuroimaging technique is high-field MRI, which, instead, trades less spatial resolution (compared to histology) for less sample-invasiveness. MRI, unlike histological neuroimaging work, can remain free from staining and labeling, and can produce truly-volumetric nervous tissue maps composed of (possibly) thousands of virtual slices. Ultra-high field MRI scanners are equipped with strong gradients, which permit access to 3D nervous tissue mesoscopic[5] bio-scale structure without the need for sample sectioning, and afford high CNS soft-tissue contrast already in-vivo[6]. *Post-mortem* high-field MRI (PMMR) can efficiently reach, though obviously at the cost of long measurement times, even higher CNS image quality[7], and obtain e.g. exquisite soft-tissue contrast and ultra-high resolution within large human brain specimens[8] (isotropic pixel sizes in the order of 50 µm), or even full rodent CNS visualizations[9] (isotropic pixel sizes in the order of 25 µm). For these reasons PMMR is finding increasing application as a tool for non-invasive virtual autopsy[10], a setting where long image acquisition times (in the order of tens of hours) are still acceptable. Interestingly, PMMR can effectively characterize microstructures even beyond the resolution limit of the imaging system. This possibility exists due to the fact that signal intensity in CNS PMMR microscopy is influenced in different ways by the complex underlying microstructural environment within nervous tissue[11] (including for example axon fibers and cell density, but also myelin, gliosis or iron content) and since different state-of-the-art MRI modalities (e.g. structural, diffusion and susceptibility scanning modes) in combination with advanced MRI data reconstruction techniques can be applied to infer specific CNS connectivity and microstructure[12]. For example, diffusion-based techniques, such as tractography, can be employed to infer the micro-connectivity of tens-of-micron-thick white-matter tracts even while employing imaging system pixel sizes only in the order of hundreds of microns[13]. These PMMR-based structural deductions are grounded on intense multimodal work, which has correlated MRI neuroimaging to ground-truth histological microstructural identifications; thanks to it, PMMR can be applied today to the study of disease-specific pathological CNS structural changes[14]. The indirect nature of these measurements, though, makes PMMR microstructural imaging intrinsically somewhat unreliable. Overall, both histology-based and MRI-based neuroimaging approaches available today still fail to capture direct and unbiased volumetric information on cellular structure and microvasculature within full-organ CNS samples.

Micro-CT technology can also play a role in CNS imaging, since, especially *post-mortem*, it can be efficiently used as a tool for 3D-virtual-histology of biological tissues[15], or to guide 3D histology[16]: produced datasets correlate well to brain[17] and spinal cord[18] tissue histology, and can be routinely applied for dissection-free volumetric investigations e.g. of CNS lesions[19], tumor[20] and micro-vasculature[21]. Traditional CT methodology, though, is based on X-ray absorption and, therefore, affords only weak soft-tissue contrast within low-absorbing biomaterials. For this reason, micro-CT neuroimaging typically involves the implementation of tailored contrast enhancement protocols, and can suffer from issues of inadequate stain penetration.

X-ray phase-contrast tomography (X-PCI-CT), for its part, is a label- and dissection-free experimental 3D imaging technique for biomedical research[22], which is emerging as an added-value technology for *post-mortem* neuroimaging. X-PCI-CT synchrotron radiation setups, by capturing X-ray phase modulations within a measured sample[23] in addition to the absorption modulations of traditional (absorption-based) X-ray CT, can achieve increased CNS soft-matter morphological contrast[24] complementary to MRI[25]. This method has been proven sensitive to the underlying cellularity of nervous and tumor tissue and to micro-vasculature[26], and, by means of sub-micron pixel size imaging systems, can provide *post-mortem* cellular-resolution visualizations[27] fit for direct dense characterizations of nervous-tissue microstructure within extended samples. Spinal neuronal-network contrast at the single-neuron and single-vessel level, obtained via X-PCI-CT, differs from advanced in-vivo (window-based[28]) and *post-mortem* (tissue-clearing-based[29]) spinal cord fluorescence microscopy (FM) technology, in that it arises in the absence of any transgenic, antibody, chemical or viral fluorescent labeling agent. In this way, label-free X-PCI-CT measurements achieve dense and direct morphological 3D maps of neural microstructural connectivity, more limited compared to molecular cell-specific FM signals in terms of the provided functional information and resolution, but also freed from the sparse-labeling and limited sample-thickness issues of FM techniques. For all these reasons, it can be said that X-PCI-CT, a sectioning- and labelling-free volumetric dense & direct high resolution method for CNS analysis, holds the potential to provide a new perspective to the study of CNS vascular[30] and neurodegenerative diseases[31,32], and supplement that of other more-established cutting-edge neuroimaging technologies.

Extensive *post-mortem* X-PCI-CT work on dissected spinal cord (SC) samples from rodent animal models has, thus far, been able to characterize anatomical intramedullary vascular structure[30,33], mesoscale white- and gray-matter nerve fibers and neuron somas[34,35], nanoscale axonal and myelin substructures[36], as well as pathological signs of various cord vascular injuries[37–39] and of spinal cord neurodegeneration[40]. These exploratory synchrotron X-PCI-CT studies demonstrate the impact this experimental technique can have on various spinal cord neuroimaging applications. And, as has already been the case for other now-established *post-mortem* CNS imaging techniques, it will be of paramount importance for the optimization of *post-mortem* spinal cord tissue contrast in X-PCI-CT images to develop adequate, goal-oriented, technique- and organ-specific CNS sample-preparation and tissue-fixation[41] protocols.

Interestingly, the X-PCI-CT research community has already evaluated several options to improve *post-mortem* X-PCI-CT soft-tissue imaging, for example by comparing ethanol vs. paraformaldehyde CNS tissue perfusion-fixation protocols[42], by testing multiple staining protocols based on iodine and heavy ions[43], and even by trying different sample embedment procedures[44] and imaging parameters[45]. In this work, we test the state-of-the-art multi-step nervous tissue sample-preparation procedure historically designed for transmission EM[46] (TEM), i.e. immersion-fixation with a combination of aldehydes, followed by osmium tetroxide impregnation. Conventional multi-aldehyde fixation with paraformaldehyde and glutaraldehyde is used to optimally preserve fast-degrading neuronal tissues, and is compatible with histological stains. Post-fixation by osmium staining, for its part, marks lipid, membrane and intracellular structures, and has traditionally been used to both enhance image contrast and further fix neuronal white-matter structure. Here, we study the influence of each of these preparation steps on intra-medullary vascular- and neuronal-network contrast within multiscale X-PCI-CT images of excised rat spinal cord samples. In this way, we hope to enhance the quality of X-PCI-CT-based microstructural CNS imaging, and thereby help direct future sample-preparation design specific for spinal-cord *post-mortem* X-PCI-CT of both small animals and human origin.

2. Materials and Methods:

2.1. Animals

For ethical reasons, spinal cords were obtained from 10 healthy wild-type Sprague-Dawley female rats already sacrificed as part of previously approved *in-vitro* neurotoxicity studies[47] at the Milano-Bicocca University. All experimental procedures involving animals were approved by the local ethical committee and performed in accordance with all European laws on animal care.

2.2. Sample preparation

Nine of the animals were sacrificed under deep anesthesia with CO_2, followed by cervical dislocation. One-centimeter-long spinal cord samples, including the lumbar enlargement, were harvested by dissecting the medullary soft-matter from the bony spinal canal. Then, the 9 extracted SC samples were fixed by immersion following three alternative protocols (a-c), which represent the three consecutive steps traditionally employed for the preservation of CNS tissue and its preparation for TEM analysis:

a. **PFA 4%**: 3 cord samples were immersed in 4% paraformaldehyde (PFA) phosphate-buffered solution 0.12M for 2 hours at room temperature.
b. **PFA 4%, Glu 2%**: 3 cord samples were immersed in PFA 4% in combination with 2% glutaraldehyde (Glu) phosphate-buffered solution 0.12M for 2 hours at room temperature.
c. **PFA 4%, Glu 2% + OsO_4**: 3 cord samples were immersed in PFA 4% in combination with Glu 2% for 2 hours at room temperature, and then post-fixed with osmium tetroxide (OsO_4) 2% in cacodylate buffer solution 0.12M for another 2 hours at room temperature.

After fixation, lumbar SC samples were divided in two portions, rostral and caudal. Rostral lumbar portions were embedded in epoxy resin for further histological analysis. Caudal lumbar portions, instead, were stored in PBS for several weeks until synchrotron-radiation X-ray phase-contrast CT imaging sessions. Right before imaging, samples were included in agar-agar gel within a sealed plastic Eppendorf tube to reduce sample dehydration and movement during CT scans. Finally, one Sprague-Dawley female rat was used to reveal the vascular structure of the spinal cord via vascular fluorescence, as explained below (see Section 2.7).

2.3. Synchrotron X-PCI-CT imaging acquisitions

X-PCI-CT scans were carried out with the propagation-based[23,48] micro-X-PCI-CT setups of two synchrotron beamlines, the biomedical beamline (ID17) of the European Synchrotron (ERSF – Grenoble, France) and the TOMCAT beamline[49,50] of the Swiss Light Source (SLS, Paul Scherrer Institute, Villigen, Switzerland). Both setups include a sCMOS PCO.Edge 5.5 (PCO AG, Germany) detector camera[51], mounted at a specific distance downstream of a sample stage, in turn equipped with translation and rotation precision motors used for fine 3D sample positioning, alignment and rotation. During scans, the sample-containing Eppendorf plastic tubes were mounted vertically on the sample stage and rotated around an axis perpendicular to the X-ray beam propagation plane, while keeping the X-ray source and detector fixed. Projection images at different angles were recorded to obtain CT datasets of the scanned samples. Three different effective detector voxel sizes, i.e. 3.0^3, 0.7^3 and 0.3^3 µm^3, were used to enable a multiscale morphological analysis of each soft-matter cord sample. The osmium-fixed samples were the only ones not imaged with the 0.3^3 µm^3 setup. The different effective voxel sizes were obtained by coupling the detector to Optique Peter™ indirect-conversion optics systems[52] affording different options for magnification (2x, 10x, 20x magnification respectively for 3.0^3, 0.7^3 and 0.3^3 µm^3 voxel systems). In all scans, the X-ray beam was shaped by tungsten slits to obtain a laminar beam, which impinged first on the samples, and then on the sCMOS detectors, equipped with 2560 x 2160 (H x V) 2D pixel matrices and either GGG, YAG:Ce (at ID17) or LuAG:Ce (at TOMCAT) scintillators to convert the X-rays into visible light. At 3.0^3 µm^3, the entire 1 cm vertical length of the rodent cord samples was covered, by acquiring CT scans at 2 vertically-contiguous heights on the sample. At higher spatial resolution, only partial vertical sample coverage was obtained by the acquired 2 to 5 vertically-contiguous stacks.

micro-X-PCI-CT with 3^3 µm^3 voxel at ID17, ESRF: these scans were performed in the imaging hutch of the ID17 beamline, around 150 m away from a wiggler X-ray source, using a quasi-parallel monochromatic 40 keV incident X-ray beam issued from a double Si(111) Laue crystal monochromator system[53]. Wiggler opening gaps were set to 55 and 45 mm respectively for w150 and w125 wiggler magnets; movable absorber filters included aluminum (1 mm) and carbon (0.8 mm). The propagation sample-to-detector distance was set to ~ 200 cm[54]. CT scan parameters included: detector exposure time per angular projection, 150 ms; detector field of view (FoV), 7.7 x 6.5 mm^2 (H x V); number of equally-spaced CT angular projections, 3000; rotation angular range, 180°;

rotation axis position, center of the CT projection (so-called full-acquisition mode); single-stack scan time, 7.5 min; number of vertical stacks, 2; total sample scan time, 15 min.

micro-X-PCI-CT with 0.7^3 µm^3 voxel at ID17, ESRF: these scans were performed in the so-called Microbeam Radiation Therapy hutch of the ID17 beamline, around 45 m away from the wigglers, using a quasi-parallel pink X-ray beam with peak at 40 keV and a broad spectrum[55]. Wiggler opening gaps were in this case set to 70 and 200 mm; movable absorber filters included aluminum (1.0 mm), cupper (0.7 mm) and carbon (1.15 mm). The propagation sample-to-detector distance was set to 50 cm. CT scan parameters included: detector exposure time per angular projection, 80 ms; detector FoV, 1.9 x 1.5 mm^2 (H x V); number of equally-spaced CT projections, 3000; rotation angular range, 360°; rotation axis position, at the edge of the CT projection (so-called half-acquisition mode); single stack scan time, 4 min; number of vertical stacks, 5; total sample scan time, 20 min.

micro-X-PCI-CT with 0.3^3 µm^3 voxel at TOMCAT, PSI: these scans were performed in the imaging hutch of the TOMCAT beamline, using a quasi-parallel monochromatic 21 keV incident X-ray beam, obtained via a W/Si double multilayer monochromator system[50]. The propagation sample-to-detector distance was set to 5 cm. CT scan parameters included: detector exposure time per angular projection, 120 ms; detector FoV, 0.86 x 0.70 mm^2 (H x V); number of equally-spaced CT projections, 3000; rotation angular range, 180°; rotation axis position, center of the CT projection; single stack scan time, 6 min; vertical stacks, 2; total sample scan time, 12 min.

2.4. X-PCI-CT image processing

Tomographic reconstructions were computed from collected projection images, using in-house software available at the respective beamlines, including the ESRF PyHST2[56] software package and the TOMCAT tomographic reconstruction pipeline[57]. Briefly, the conventional filtered-back projection algorithm was used after application of the single-distance Paganin[58] phase-retrieval algorithm, in order to transform image edge-enhancement into pseudo-quantitative area-contrast (phase-images). We removed cupping artifacts, likely due to the local-tomography configuration of CT scans (i.e. with sample sizes larger than the detector FoV), via slice-by-slice normalization: CT images were divided by their Gaussian-blurred version (ImageJ[59] Gaussian filter, sigma: 50 pixels), thereby suppressing the low-frequency image background. Moreover, we removed most CT ring artifacts by means of a published ring-removal approach[60], based on the ring-reducing subtraction of angularly filtered CT images from the original ones. Maximum intensity projections (MIPs) were computed by summing 50-100 consecutive reconstructed CT slices, using the ImageJ maximum intensity z-projection function, which projects 3D bright features onto a 2D plane. Minimum intensity projections (mIPs) were obtained in a similar way, but using the minimum intensity z-projection function instead, and thereby projecting dark image features. Different ImageJ preset lookup tables (LUTs) were used to recolor CT data (e.g. Viridis & Fire LUTs) and highlight different cord microstructural features. 3D renderings of CT data were computed using the commercial software VG Studio Max 3.2 (Volume Graphics GmbH, Heidelberg, Germany). Threshold-based segmentation approaches were used to extract cellular vs. vascular features, and the semi-transparent ‘X-ray’ 3D rendering algorithm, available in VG Studio Max, was chosen to render the segmented structures in 3D.

2.5. X-PCI-CT image analysis

Using an automatic threshold algorithm (Max Entropy[61]) available in ImageJ, we could segment 3D masks of cell-like features from 0.7^3 and 0.3^3 μm^3 voxel datasets. The same auto-threshold algorithm was applied to datasets from all three sample-preparation group. Obtained masks included all closed objects above the automatically-determined threshold (mainly cell somas, but also interrupted portions of neighboring blood-vessels). These masks were then analyzed with the '3D Object Counter' ImageJ plugin[62] to quantify the volumes of unconnected segmented objects, and thereby obtain distributions of cell-like object sizes, expressed as equivalent-sphere diameters (after assumption of a spherical object shape). Manual threshold selection, instead, was used to extract 3D masks of vascular features only from both 0.7^3 and 0.3^3 μm^3 voxel datasets. These vessel network masks were analyzed with the 'Local Thickness' ImageJ plugin[63], to obtain quantitative distributions of vascular thickness sizes. Violin plots of extracted cellular size and vascular thickness distributions were produced with the commercially available software GraphPad Prism (GraphPad Prism 8.0.0, GraphPad Software Inc., San Diego, CA, USA).

2.6. High-field MRI

The same Eppendorf plastic tubes used for X-PCI-CT, containing the agar-embedded rodent cords, were also used to acquire *post-mortem* high-field MRI with a preclinical 9.4 T MRI scanner (BioSpec 94/21; Bruker Biospin, Ettlingen, Germany). Axial spinal cord images were collected using a transceiver cryogenic quadrature RF surface probe (CryoProbe, catalog number Z125365, Bruker Biospin, Ettlingen, Germany). Two osmium-free samples were imaged with this MRI setup, one from the PFA 4% group and one from the PFA 4%, Glu 2% group. The acquired contrast-agent free MRI datasets were obtained using the following parameters: sequence, 3D FISP; repetition time (TR), 30 ms; echo time (TE), 11 ms; excitation pulse angle 20°; FOV, 8 x 8 x 6 mm^3; acquisition matrix, 400 x 400 x 300 voxels; voxel size, 20 x 20 x 20 μm^3; number of averages, 16; scan time, ~19 hrs.

2.7. Histological stainings

Briefly, resin embedded samples were cut on a microtome (Leica RM2265, Leica Microsystems GmbH, Wetzlar, Deutschland) into 1.5-µm-thick sections, and then stained with toluidine blue. Due to the absence of osmium impregnation, which normally aids membrane preservation, we were obliged to use (non-standard) high staining times for both the PFA 4% sample preparation group (5 min) and the PFA 4%, Glu2% sample preparation group (2 min). A motorized Olympus BX63 equipped with DP80 camera and software cellSens (Shinjuku Monolith, Tokyo, Japan) was used for analyzing the slices and acquiring 20x reconstructed images after photo stitching.

Moreover, one healthy Sprague-Dawley rat, not involved in the X-PCI-CT measurements, was used to collect vascular fluorescence data. Briefly, after deep animal anesthesia with ketamine and xylazine, a dose of 2 µgr/µl Tomato Lectin[64] (FITC conjugated, Sigma-Aldrich, Saint Louise, USA) was injected into the proximal tail vein of the rat 2 minutes before its perfusion with PFA 4%. The dissected spinal cord was collected and a 0.1 mm slice observed using a Meta710 confocal microscope (Zeiss, Oberkochen, Germany).

3. Results

The 3D synchrotron X-PCI-CT data collected with the 3.0^3 µm^3 voxel propagation-based setup (**Fig. 1**) permits a side-by-side qualitative comparison of image quality between each of the three steps in the rodent spinal cord sample preparation procedure, i.e. paraformaldehyde 4% (PFA 4%) fixation vs. PFA 4% + glutaraldehyde 2% (PFA 4%, Glu 2%) fixation vs. PFA 4%, Glu 2% + osmium tetroxide 1% impregnation (PFA 4%, Glu 2% + OsO_4). Within axial views of the medulla spinalis (**Fig. 1a**), all three sample preparations allow an at-least partial delineation of gross full-organ spinal cord anatomy, including spinal fissures, septa and sulci, the central canal, spinal funiculi, (superficial) extra-medullary spinal arteries and the anterior, lateral and posterior gray horns. Moreover, signs of intra-medullary vascular (red arrows in **1a** zooms 3x) and cellular (yellow arrows, likely motor neurons, in **1a** zooms 3x) microstructure are already visible at this resolution in all sample types, without need for vascular contrast-agent injection. OsO_4 post-fixation stains myelin sheaths within nerve fibers; this impregnation leads to the direct 3D visualization via X-PCI-CT of both (hypo-dense) unmyelinated axons (**Suppl. Fig. 1**) and osmicated (hyper-dense) myelinated nerve fibers (magenta arrows point to nerve fibers in **Fig. 1a** Zooms 3x, **Suppl. Fig. 1**).

In terms of image area contrast, some gray vs. white matter contrast is evident in all measured medullary axial and coronal SC virtual CT slices (**Fig. 1a-b**). Moreover, within osmium-free cords (PFA 4% and PFA 4%, Glu 2% preparation groups) the brightest image gray-level values arise from non-perfused blood-filled vessels and their thick endothelial cell walls, followed in order by the gray levels of cell-soma structures, of gray-matter parenchyma and, last, of white matter. The addition of osmium (PFA 4%, Glu 2% + OsO_4 preparation group), for its part, leads to an inversion of intramedullary nervous tissue contrast. The osmium impregnation itself becomes the highest-Z material present, leading to enhanced white-matter brightness compared to gray matter tissue intensity. This inversion influences also the signal intensity within cell-like structures (zooms 3x in **Fig. 1a**, inserts in **Fig. 1b**), with neurons in osmicated samples appearing as the darkest structures, compared to neurons in staining-free samples, which instead look mildly denser than surrounding neuropil. Vascular feature gray-level brightness, instead, seems unperturbed by the osmium metal fixative.

Maximum and minimum intensity projection (MIP and mIP, see **Methods**) images were calculated to highlight and compare the volumetric development of respectively the brightest and darkest image features within different extended axial and sagittal CT data volumes (**Fig. 1 c-d**). In these pseudo-volumetric maps, we can observe extended vascular tree morphology (red arrows) as well as local cyto-architecture (yellow arrows) within samples of all preparation groups. Within MIP datasets of osmium-free samples (PFA 4% and PFA 4%, Glu 2% preparation groups), extensive deep micro-vasculature can be recognized within both gray and white-matter tissues. MIPs of osmium-stained medullas, instead, allow good renderings of vascularization within gray-matter, but only little vascular structure visualization within the white-matter. In its place, they portray the detailed volumetric structure of white-matter nerve bundles, e.g. the pseudo-3D out-branching of individual white-matter fibers (magenta arrows) toward more-internal medullary gray-matter tissue (**Figs. 1d, 2d-e, 2i**). Deep motor neuron populations are revealed within MIP maps of osmium-free spinal cords and within mIP of osmicated ones (yellow arrows, **Fig. 1d**).

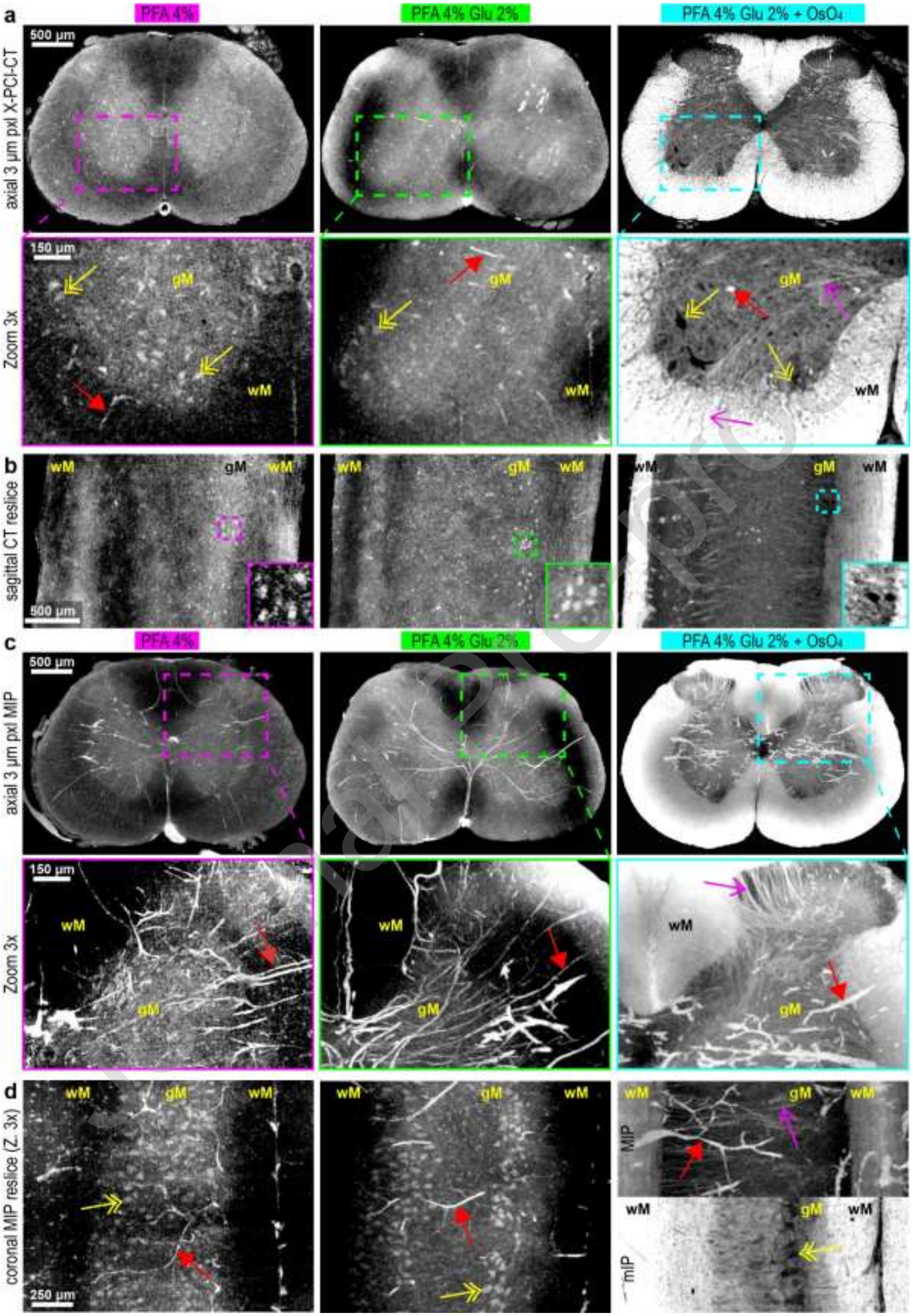
a
PFA 4%
PFA 4% Glu 2%
PFA 4% Glu 2% + OsO4
500 µm
axial 3 µm pxl X-PCI-CT
150 µm
Zoom 3x
gM
wM
b
sagittal CT reslice
wM
gM
wM
500 µm
c
PFA 4%
PFA 4% Glu 2%
PFA 4% Glu 2% + OsO4
500 µm
axial 3 µm pxl MIP
150 µm
Zoom 3x
wM
gM
d
coronal MIP reslice (Z. 3x)
wM
gM
wM
250 µm
MIP
mIP

FIGURE 1. Impact of aldehyde fixation and osmication of rat spinal cords on X-PCI-CT with 3.0^3 µm^3 voxels. Representative (**a**) axial and (**b**) sagittal views from *post-mortem* 3.0^3 µm^3 voxel 3D X-PCI-CT datasets of rodent spinal cord specimens fixed by immersion respectively with paraformaldehyde 4% only (PFA 4%), with PFA 4% and glutaraldehyde 2% (PFA 4%, Glu 2%), and with PFA 4%, Glu 2% plus post-fixation in osmium tetroxide (PFA 4%, Glu 2% + OsO_4). Zoomed 3x images in (**a**) show axial gray vs. white matter contrast (gM, wM), and vascular (red arrows), cellular (yellow arrows) and nerve fiber (magenta arrows) microstructures. Inserts in (**b**) show sagittal cellular features. Note nervous tissue and structure contrast inversion in the osmicated samples. (**c**) Axial and (**d**) zoomed 3x sagittal MIP maps (plus one mIP map) highlight bright (dark) features pseudo-volumetrically. Again, vascular, cellular and fiber structure detail within gM and wM is indicated with red vs. yellow vs. magenta arrows. Agar gel background was masked in all presented CT images for clarity.

X-PCI-CT imaging data on extended sections of osmium-stained (PFA 4%, Glu 2% + OsO_4) cord medullas (**Fig. 2**) confirms that an efficacious homogeneous penetration of the Os metal within small rodent spinal cord samples was obtained, leading to very high-contrast nervous tissue visualizations. These measurements enable the 3D exploration of micrometric medullary anatomy in axial, sagittal and coronal views (**Fig. 2a**). Moreover, pseudo-volumetric MIP- and mIP-based rendering of vascular, fiber (**Fig. 2b**) and cellular (**Fig. 2c**) structures, well-visible in zoomed multi-view displays (**Fig. 2d-f**), demonstrate the ability of the method to capture extended feature-specific 3D networks deep within soft-matter CNS tissue. mIP maps of dark cellular features can be recolored to mimic cellular fluorescence microscopy data (**Fig. 2g**), and their virtual re-slicing in all 3 orthogonal planes proves that dissection-free full-organ rodent cord 3D cellular imaging is possible with this sample preparation and imaging approach. Moreover, the differential recoloring of MIP vs. mIP maps (**Fig. 2h**) makes it evident that the achieved image contrast within these contrast-enhanced osmium-stained medullas is sufficient to separate, and independently study, bright hyper-dense vasculature and fiber networks, recolored to red-violet tones, vs. dark hypo-dense neuron populations, recolored to green-yellow tones. The high level of organ-wide CNS structure morphological detail attainable is evident in the zoomed-in displays (**Fig. 2i-j**), extracted from the full-sample MIP and mIP maps (**Fig. 2b-c**):

the fine structure of individual osmium-stained nerve fibers, of individual intra-medullary micro-vessels (**Fig. 2i**), and even of individual differently-sizes neurons and their somatic and dendritic sub-structure (**Fig. 2j**), appears quite well defined.

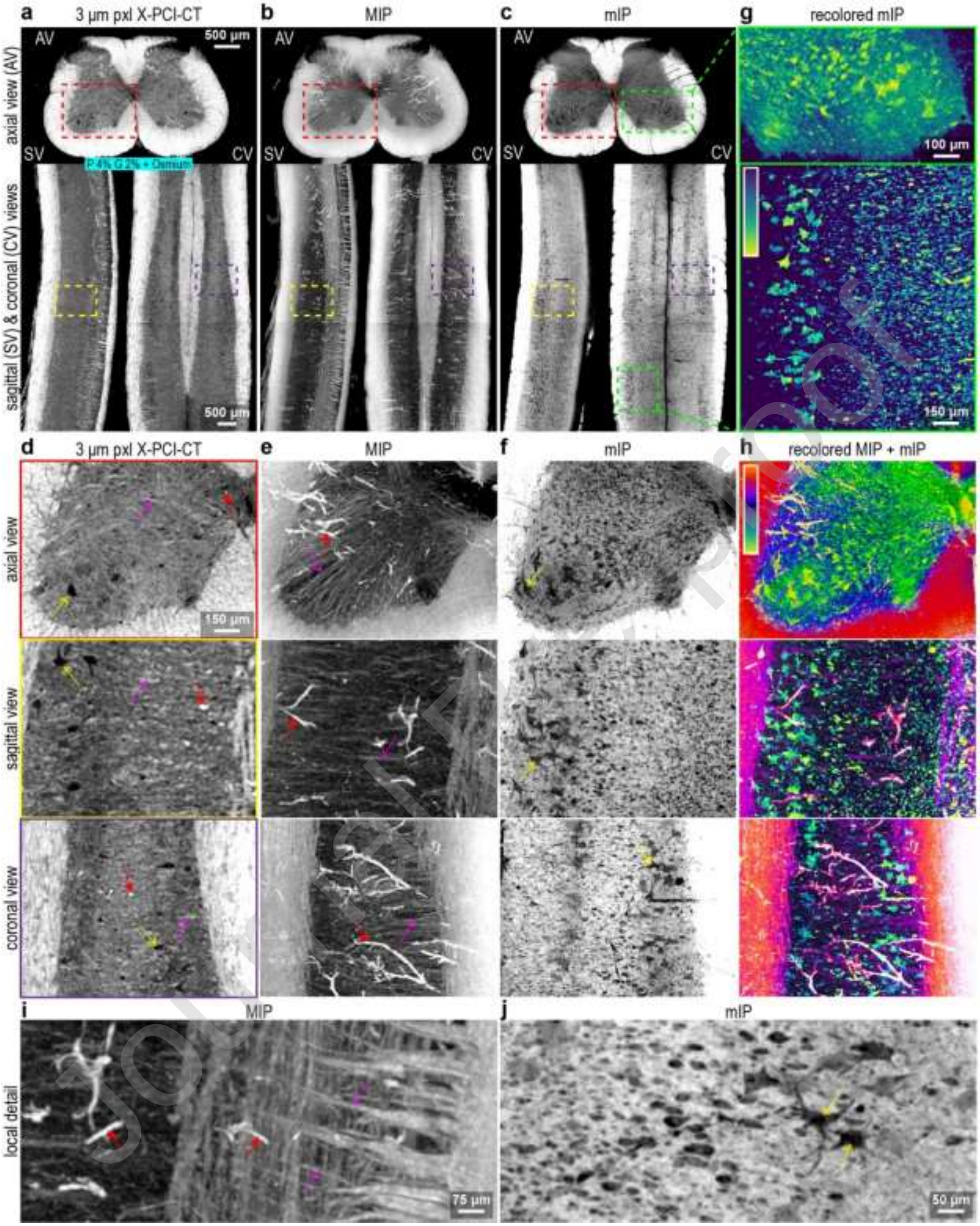

FIGURE 2. X-PCI-CT with 3.0^3 µm^3 voxels of osmicated rat spinal cords. (**a**) CT vs. (**b**) MIP vs. (**c**) mIP X-PCI-CT maps showing axial, sagittal and coronal views of a PFA/Glu aldehyde-fixed & osmium-stained rat spinal cord (PFA

4%, Glu 2% + OsO4 sample preparation group). (**d-f**) axial, sagittal and coronal zoomed (2x) views of image data from the color-associated dashed rectangles in (**a-c**). Red, yellow and magenta arrows indicate respectively vascular, cellular and fiber microstructure. (**g**) Zoomed views of mIP maps within the connected dashed rectangles in (**c**), recolored with the 'Viridis' LUT. (**h**) Sum of the MIP data in (**e**), recolored with the 'Fire' LUT, plus the mIP data in (**f**), recolored with the 'Viridis' LUT. In (**g**-**h**) color bars specify the recoloring of low-to-high CT gray-levels. (**i-j**) 4x ultra-zooms of (**i**) MIP and (**j**) mIP data, extracted respectively from (**b**) and (**c**), display detailed local morphology of vascular (red arrows), cellular (yellow arrows) and fiber (magenta arrows) microstructure. Agar gel background was masked in all presented CT images for clarity.

To further explore the potential of each sample preparation method for morphologic 3D spinal cord X-PCI-based neuroimaging, we collected sub-micron voxel size synchrotron X-PCI-CT data on selected rat cord samples (**Fig. 3**). 0.7^3 μm^3 voxel MIP and mIP data shows that the feature contrast already observed in micro-CT datasets (**Fig. 1**) can be similarly recapitulated also in sub-micron CTs. Again, vasculature generates the brightest voxel values in all cords, and osmium-stained nervous tissues produce inverted gray vs. white-matter contrast compared to unstained ones. Motor neuron somas within gray-matter horns, in particular, appear within aldehyde-only fixed samples (PFA 4% and PFA 4%, Glu 2% preparation groups) as mildly hyper-intense pyramidal structures containing bright nucleoli, whereas as dark similarly-shaped features containing dark nucleoli within osmium-stained samples (PFA 4%, Glu 2% + OsO_4 preparation group) (**Fig. 3a**). Furthermore, since they have slightly-differing gray-levels, cellular vs. vascular anatomical structures can be manually segmented based on their gray-level threshold, enabling the color-coded 3D rendering and volumetric differentiation of cellular and vascular features present within extended nervous-tissue datasets (**Fig. 3b**, **Suppl. Fig. 2a-c**).

Non-osmicated medullas (PFA 4% and PFA 4%, Glu 2% preparation groups) were analyzed also with a 0.3^3 μm^3 voxel X-PCI-CT setup (**Fig. 3c**) in order to verify cellular-level tissue preservation and demonstrate that sub-cellular-level structural visualizations are achievable by *post-mortem* sub-micron X-PCI-CT. At this ultra-high resolution, we recognize single neuronal cells perfused by surrounding micro-vasculature, as well as some intra-cellular structure: cell bodies of individual motor neurons, including their bright/dense cell nucleoli and their dendritic components, as well as other smaller likely glial cells, are visible deep within un-sectioned SC samples (from both types of aldehyde-fixation) without need for staining or contrast agent injection (**Fig. 3c**). Furthermore, these microstructural data show that both fixation procedures preserved nervous tissue structural integrity. Therefore, they could be used to visualize intra-cord vascular and cellular networks in 3D (**Fig. 3d**, **Suppl. Fig. 2d-e**), by applying manual threshold segmentation approaches to separate vascular vs. cellular features based on their gray-level. These 3D representations characterize the volumetric arrangement of local cells and capillaries, and even display some intra-cellular detail, e.g. nucleolar detail.

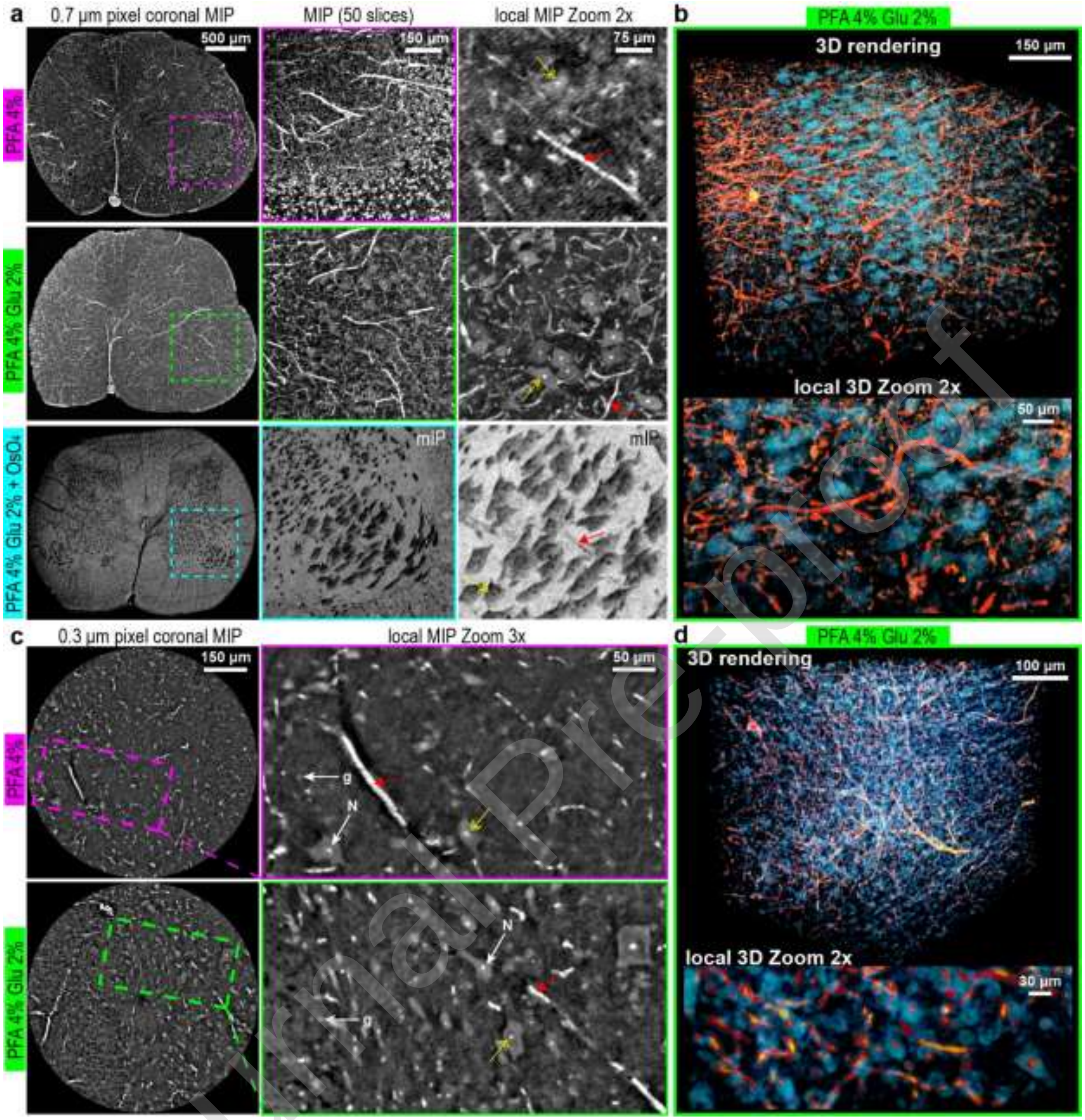

FIGURE 3. Impact of aldehyde fixation and osmication of rat spinal cords on X-PCI-CT with sub-micron voxels. (**a**) Representative axial views from *post-mortem* 0.7^3 µm^3 voxel 3D X-PCI-CT MIP datasets of rat spinal cord medullas fixed by immersion respectively with paraformaldehyde 4% only (PFA 4% preparation group), with PFA 4% and glutaraldehyde 2% (PFA 4%, Glu 2% preparation group), or with PFA 4%, Glu 2% plus post-fixation in osmium tetroxide (PFA 4%, Glu 2%, OsO$_4$ preparation group). 50-slice MIP maps (or mIP maps for the third group), computed from image data within the dashed rectangles in the left-most panel column, highlight bright (or dark in the mIPs) features pseudo-volumetrically. Zooms 2x show local vascular and cellular detail, labelled respectively with red and

yellow arrows. (**b**) 3D rendering, after threshold-based segmentation, of a 100-slice 0.7^3 μm^3 voxel CT dataset from a PFA 4%, Glu 2% preparation group spine, showing vascular features, colored in shades of red, and cellular features, colored in shades of blue. The 2x zoom shows 3D detail of local medullary tissue microstructure. (**c**) Representative axial 0.3^3 μm^3 voxel *post-mortem* local X-PCI-CT MIP data of rat cords fixed with PFA 4% or PFA 4% + Glu 2% in combination. Local MIP zooms (3x) visualize vascular vs. cellular detail (red vs. yellow arrows), neurons (N) vs. glial cells (g). Note that intra-cellular microstructure is resolved here. (**d**) 3D rendering, obtained as in (**b**), of a 150-slice 0.3^3 μm^3 voxel X-PCI-CT dataset of fixed medullary tissue from a PFA 4%, Glu 2% preparation group specimen. Note that bright/dense intra-cellular nucleoli are rendered in red, like local micro-vasculature, and neuronal cell bodies in blue. Agar gel background was masked in all CT images for clarity.

The collected multiscale 3D X-PCI-CT datasets imaging CNS tissue seem well suited for structural analyses of various kinds. Here, by selecting and analyzing volumes of lateral gray horn spine tissue data, we performed a proof-of-principle quantification of cell-like and vascular image features (**Fig. 4**, **Suppl. Fig. 3**). All three spinal cord sample-preparation procedures were included in the analysis of 0.7^3 μm^3 data (**Fig. 4a**), whereas the quantification of 0.3^3 μm^3 data (**Suppl. Fig. 3a**) was limited to fixed unstained cord samples (PFA 4% and PFA 4%, Glu 2% preparation groups). Procedurally, from the gray-level datasets (**Fig. 4a, Suppl. Fig. 3a**), masks containing cell-like microstructures (**Fig. 4b, Suppl. Fig. 3b**) were extracted via an automatic[61] threshold-based segmentation technique, masks containing vascular features (**Fig. 4c, Suppl. Fig. 3c**) instead via manual thresholding (see **Methods**). The applied auto-threshold algorithm, which extracts all types of closed objects within a certain gray-level regime, did not always discriminate well between voxels pertaining to hyper-dense cell somas, and neighboring voxels, pertaining to local vasculature. This is especially evident in the segmentations obtained from 0.7^3 (**Fig. 4b**) and 0.3^3 μm^3 (**Suppl. Fig. 3b**) voxel data of PFA/Glu samples, due to the high vascular-feature contrast in these images. Therefore, cell-like object masks contained also some extraneous local vessels. Since they were obtained manually, vascular masks (**Fig. 4c**, **Suppl. Fig. 3c**), instead, did not contain extraneous objects.

ImageJ[59] implementations of established 3D object measurement algorithms[62,63] were used to quantify the size of the extracted cell-like objects (**Fig. 4b, Suppl. Fig. 3b**) and the thickness of the extracted vasculature (**Fig. 4c, Suppl. Fig. 3c**), obtaining distributions for each type of sample preparation. The analysis of cell-like microstructure (graphs in **Fig. 4b, Suppl. Fig. 3b**) measured that a majority of detected cell-like objects has diameters falling within a 2-20 microns range, which is appropriate for various types of rodent neural cells[65]. Vessel thickness distributions (graphs in **Fig. 4c, Suppl. Fig. 3c**), for their part, measured detected vascular diameters in the 2-10 microns range. Obviously, higher-resolution datasets (**Suppl. Fig. 3**), which enable the detection of smaller objects than lower-resolutions scans (**Fig. 4**), overall led to cell-like objects being quantified as smaller and to vasculature-like tubular structures as thinner. Overall, these microstructure quantifications resulted in comparatively quite similar distributions for each of the three different cord sample preparation protocols (**Fig. 4b-c**, **Suppl. Fig. 3**).

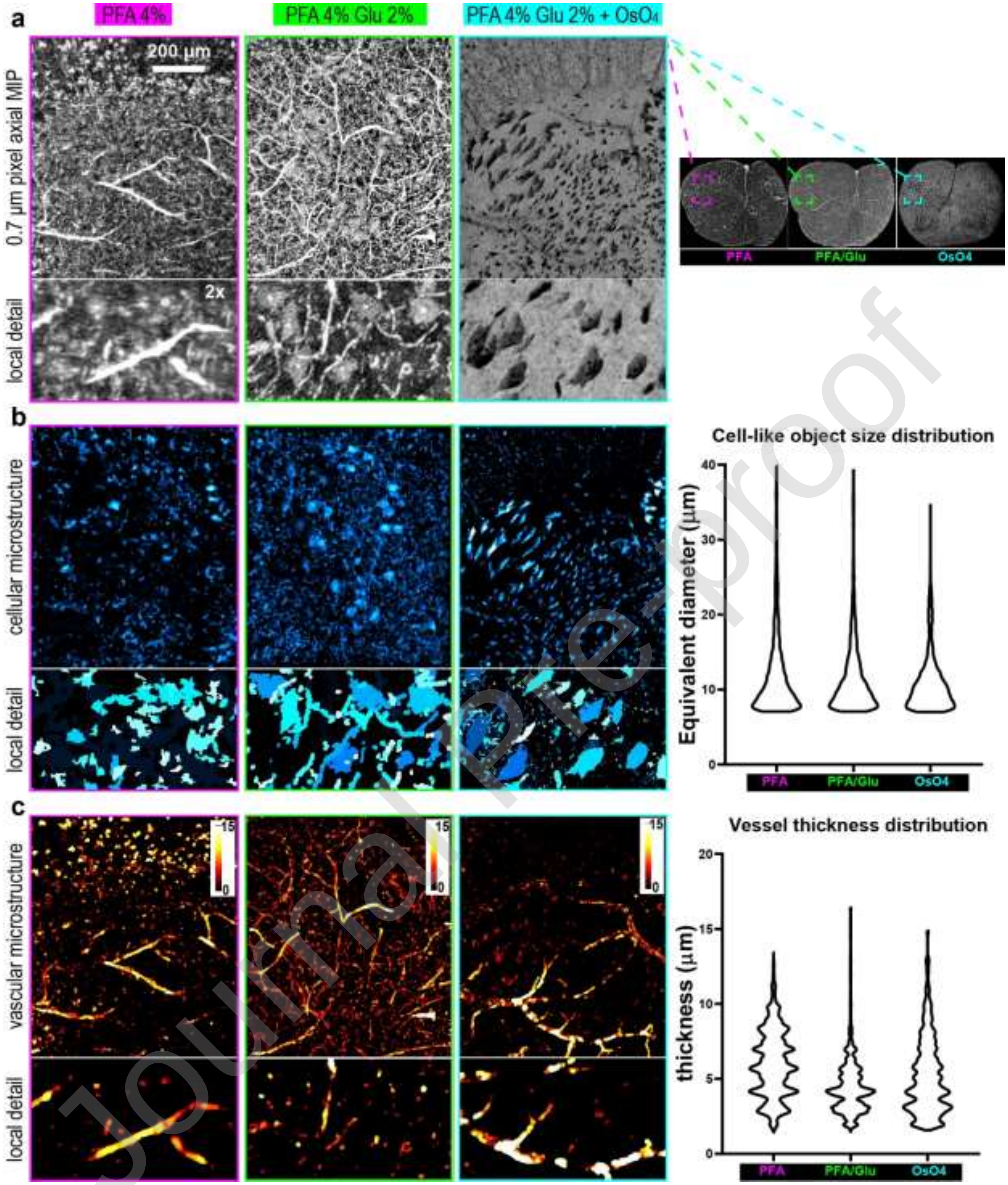

Figure 4. Quantification of cellular and vascular parameters using X-PCI-CT data with 0.7^3 µm^3 voxels. (**a**) 0.7^3 µm^3 voxel axial X-PCI-CT MIP data of lateral horn gray-matter tissue, collected from cords prepared with all three different sample-preparation protocols (PFA fixation vs. combined PFA/Glu fixation vs. PFA/Glu fixation + OsO_4 impregnation). (**b**) recolored masks of X-PCI-CT MIP data from (**a**), segmented via an automated threshold algorithm

(see **Methods**) to extract cell-like microstructure. Local (2x zoomed) mask detail is also displayed to better visualize the result of the segmentations. Especially in the PFA/Glu data, some of the segmented objects or voxels actually pertained to vascular structure. Violin plots report size distributions obtained by extracting the equivalent diameter of each distinct 3D object in the masks, quantified via an image analysis plugin of ImageJ specific for populations of 3D objects (see **Methods**). (**c**) quantitatively-recolored masks of X-PCI-CT MIP data from (**a**), segmented by manual threshold selection to extract vascular microstructure. Color-coding quantifies the internal thickness of tubular structures (calibration bar in µm), computed with an ImageJ image-analysis plugin specific for tubular 3D structures (see **Methods**). Local mask detail is displayed to better visualize the goodness of the segmentations. Violin plots report vessel thickness distributions, obtained by combining all voxel values in the corresponding image masks in (**c**).

To better benchmark our multiscale *post-mortem* spinal cord X-PCI-CT imaging results (**Fig. 1-3**), we imaged the same (caudal) lumbar SC samples also with a 9.4 T PMMR setup, i.e. state-of-the-art non-invasive volumetric imaging technology. Moreover, we analyzed the set-aside rostral SC samples with traditional toluidine blue histology in combination with optical microscopy (OM), i.e. state-of-the art 2D cellular imaging technology. A side-by-side comparison of histological vs. X-PCI-CT-based vs. MRI-based medullary axial views is presented in **Fig. 5**. The 3^3 µm^3 voxel X-PCI-CT panels of non-osmicated cords (PFA 4% and PFA 4%, Glu 2% preparation groups) display the potential of this technique for a staining-free full-organ 3D examination, which detects local vascular and cellular microstructure (**Fig. 5a-b**). Comparatively, the 20^3 µm^3 voxel PMMR data show superior gray vs. white matter contrast but also an only at-best pre-cellular resolving power, leading to only partial visualizations of underlying SC cellular and fiber structure (see inserts in **Fig. 5a-b**). Cord impregnation with osmium (PFA 4%, Glu 2%, OsO_4 preparation group), for its part, leads to much-enhanced white-matter contrast within X-PCI-CT data (**Fig. 5c**), as well as a clear delineation of white-matter fiber structure, surpassing the quality of the white-matter visualizations recapitulated in both X-PCI-CTs and PMMR images (both 3D FISP and 3D FISP phase maps, **Fig. 5a-c**) of non-osmicated SC samples.

The full medullary views of toluidine blue-stained 2D histology data (**Fig 5a-c**) served, first of all, as ground-truth for the correct interpretation of the 3D imaging datasets, and were used to assess the white vs. gray matter contrast obtained via X-PCI-CT and PMMR: though histological toluidine blue staining seems undeniably superior in terms of nervous-tissue differentiation capability, especially after osmium post-fixation, acceptable histology-like macroscopic gray vs. white-matter tissue delineation seems indeed possible also via both virtual-histological imaging techniques. Once again, the most striking differences can be recognized in the unequal possibilities for cellular-resolution imaging of the three techniques (inserts in **Fig. 5a-c**). Already without need for further magnification, the histological optical-microscopy approach affords the most detailed cellular-level visualizations, with boundaries of individual neural cells appearing very well defined by the histological stain. Label-free density-based detection of cellular structure by X-PCI-CT, for its part, enables at least some cell-soma visualization already within isotropic 3.0^3 μm^3 voxel data, though at the price of less cell-structure boundary definition compared to the histological approach. Last, the isotropic 20^3 μm^3 voxel PMMR data, instead, comes completely short of resolving any well-defined cell structure, with underlying cord structural micro-anatomy only vaguely perceptible within pixelated data visualizations.

Moreover, the toluidine blue histology, collected from the same organs used to produce the samples analyzed via X-PCI-CT, was essential to verify and compare (at the cellular scale) the degree of nervous-tissue preservation in the three different rodent cord sample groups. Overall, gross anatomical structures (e.g. gray-matter horns, white matter columns, etc.) within spinal cord tissues from all three sample-preparation groups (PFA 4% vs. PFA 4%, Glu2% vs. PFA4%, Glu2% + OsO_4) are well preserved and easily distinguishable within 2D toluidine blue histological slices (first column in **Fig. 5a-c**). Nevertheless, higher-magnification OM images of the same sections (**Fig. 5d-e**, **Suppl. Fig. 4**) provide the cyto-structural information necessary to observe protocol-dependent differences in cellular-level tissue preservation within both white-

(**Fig. 5d**) and gray-matter (**Fig. 5e**) tissues areas. Evident similarities and differences between fixation protocols can be noted: sub-cellular motor neuron structure within ventral horns, such as nuclei and nucleoli, are well distinguishable in histological slices from all preparation cases; unsurprisingly, they are thus detectable via X-PC-CT (yellow arrows in **Fig. 5d**). Also motor efferent nerve fibers, passing through the white matter, can be recognized in histology data from all three cases, and are visible – though only barely – also within X-PCI-CT data (azure arrows in **Fig. 5e, Suppl. Fig. 4b**). Upon closer inspection of the histological data, however, it is evident that samples from the PFA 4%, Glu 2% + OsO_4 group are the best preserved ones: osmication, which aids the fixation of lipid-rich cell structures (e.g. cellular membranes) in this group, visibly marks myelination at the level of single nerve sheaths (**Suppl. Fig. 4**). Instead, the poor lipid preservation in non-osmicated samples (PFA 4% and PFA 4%, Glu2% samples-preparation groups), which imposed higher staining times for acceptable cellular structure during preparation (see **Methods**), is responsible for the excessively dark blue-staining of motor neurons in the non-osmicated slices compared to neurons in osmicated ones (**Fig. 5d**). Moreover, such lipid wash-out appears especially evident in dorsal horn neuropil, where sensory afferent fibers were found to be well preserved only within osmicated samples (green arrow in **Suppl. Fig. 4a**). This histological finding explains the almost complete lack of fiber visualization in dorsal horn X-PCI-CT images of non-osmicated cords, and instead the quite rich fiber networks visible in osmicated ones (green arrow in **Suppl. Fig. 4a**). Last, the lack of complete lipid fixation determines also the scarcity in dark blue myelin sheaths, which can be observed around axons in white matter areas within PFA 4% and PFA 4%, Glu2% samples (magenta arrows in **Fig. 5e**, **Suppl. Fig. 4b-c**). Such a poor lipid-layers preservation is thus likely at least partially responsible for the overall weak structural definition and contrast of white-matter structures (e.g. minute individual sections of nerve fibers) within X-PCI-CT images of non-osmicated SC samples (magenta arrows in **Fig. 5e**, **Suppl. Fig. 4b-c**).

Much subtler differences can be appreciated between the PFA-only group aldehyde fixation group and the mixed PFA/Glu, with the latter expectedly preserving the morphology of individual white-matter bundles slightly better than the former (**Fig. 5e**). Overall, the comparison of cellular toluidine blue histology to sub-micron X-PCI-CT data (**Fig. 5d-e**) shows that, at sub-micron resolutions, X-PCI-CT can provide cellular and micro-vascular visualizations comparable to histological ones (**Fig. 5d**) already within non-osmicated cords. Distinctive of X-PCI-CT, though, is that these structures reside deep within un-sectioned rodent spinal medullas and are detected based on local density levels without need for any cellular staining or labeling. Addition of osmium impregnation in pre-imaging protocols leads to superior lipid fixation within samples, and thus to enhancement of contrast and structural detail in X-PCI-CT data of white-matter tissues (magenta arrows in **Fig. 5**, **Suppl. Fig. 4b-c**). Interestingly, though, the osmium reduces the visibility of individual blood-filled sharp-boundary-rich micro-vessels, which are clearly identifiable only in data from osmium-free samples (red arrows in **Fig. 5**, **Suppl. Fig. 4a**).

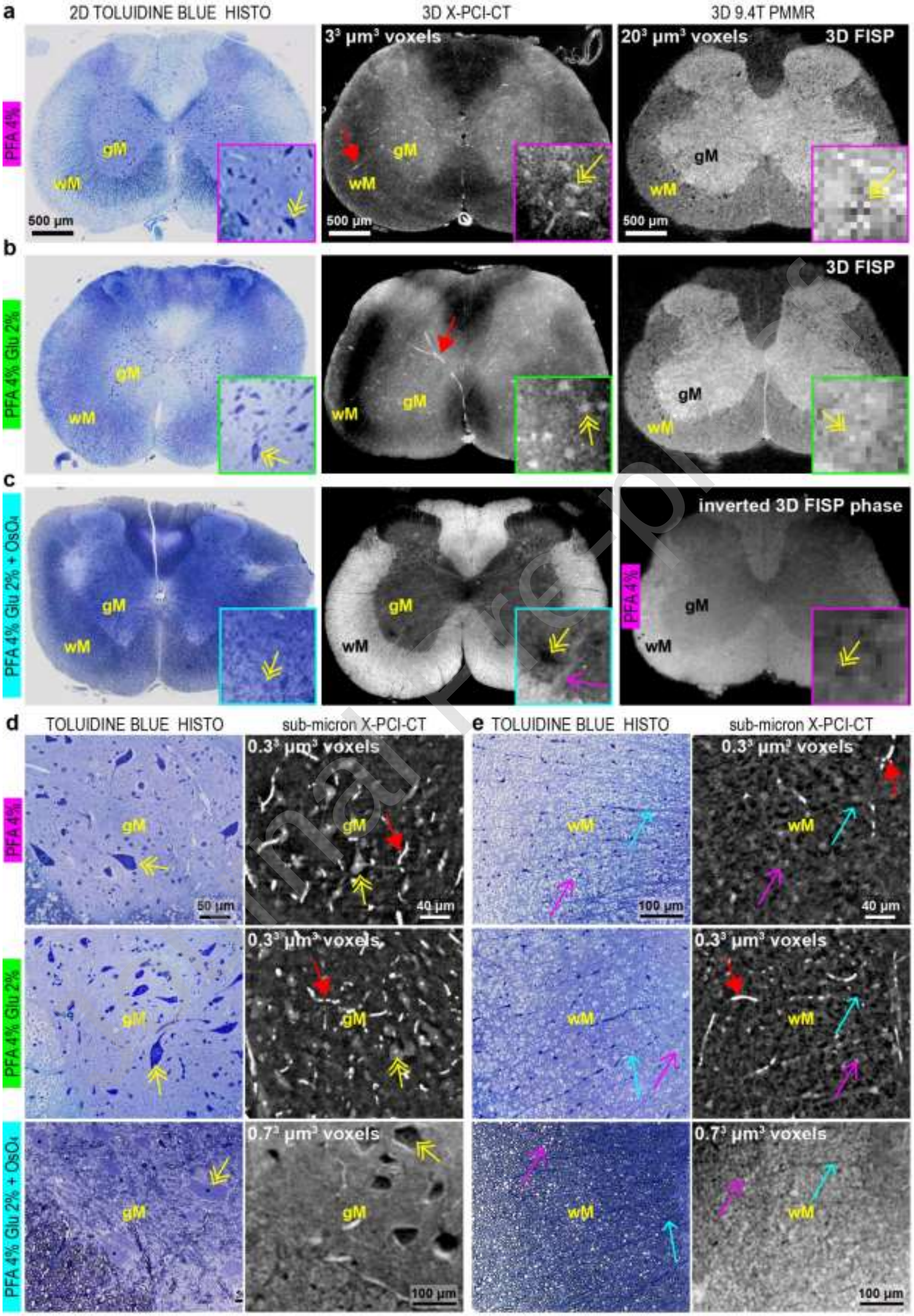
a
2D TOLUIDINE BLUE HISTO
3D X-PCI-CT
3D 9.4T PMMR
PFA 4%
3³ μm³ voxels
20³ μm³ voxels
3D FISP
gM
wM
500 μm
b
PFA 4% Glu 2%
3D FISP
gM
wM
c
PFA 4% Glu 2% + OsO₄
inverted 3D FISP phase
PFA 4%
gM
wM
d
TOLUIDINE BLUE HISTO
sub-micron X-PCI-CT
0.3³ μm³ voxels
50 μm
40 μm
0.7³ μm³ voxels
100 μm
e
TOLUIDINE BLUE HISTO
sub-micron X-PCI-CT
0.3³ μm³ voxels
0.7³ μm³ voxels
100 μm
40 μm
gM
wM

Figure 5. 3D X-PCI-CT vs. 3D PMMR and 2D cellular histology. (**a-c**) Comparison of rodent spinal medulla axial views, obtained via 2D toluidine blue histology vs. 3^3 µm^3 voxel 3D X-PCI-CT vs. 20^3 µm^3 voxel 3D 9.4 T PMMR (3D FISP sequence), using cords prepared *post-mortem* via (**a**) PFA 4%, or (**b**) PFA 4%, Glu 2%, or (**c**) PFA 4%, Glu 2% fixation + Osmium impregnation. In (**c**), the PPMR 3D FISP phase image was acquired from a PFA 4% sample, and inverted to best match the inverted-contrast of osmicated cord X-PCI-CT data. Note the display of gray-matter (gM) vs. white-matter (wM) contrast in all cases, and of high-contrast vascular structure only in X-PC-CT datasets of non-osmicated samples (red arrows). Inserts (3x zooms of the larger images) show differences between techniques and preparations in the visualization of cellular structure (yellow arrows) within ventral gray-horn tissues. X-PCI-CT of osmicated cords also displays local enhanced white-matter fiber delineation (magenta arrow). (**d-e**) Magnified (20x with respect to data in (**a-c**)) optical microscopy data of toluidine blue-stained histological slices vs. isometric sub-micron (0.7^3 to 0.3^3 µm^3 voxel) X-PCI-CT data of un-sectioned cord tissue, centered respectively on (**d**) ventral horn gM and (**e**) lateral column wM tissues. Sample data from all three sample-preparation protocols as in (**a-c**) are included in (**d-e**). Note the abundance of micro-morphology detail, with vascular vs. cellular vs. white-matter (e.g. minute individual sections of nerve fibers) structures indicated respectively by red vs. yellow vs. magenta arrows, as well as motor efferent fibers passing through the white matter (marked with azure arrows). Agar gel background was masked in several of the presented CT and MRI images for clarity.

Last, we compared multiscale X-PCI-CT data (**Fig. 6a-b**), obtained by scanning the same staining-free PFA/Glu-fixed rodent spinal cords with 3 to 0.3^3 µm^3 voxel setups in succession, to cutting-edge neuroimaging technology for the investigation of cellular and vascular microstructure within CNS tissue (**Fig. 6c-d**), i.e. respectively to traditional 2D histology (**Fig. 6c**) and 3D confocal fluorescence microscopy (**Fig. 6d**). Multiscale X-PCI-CTs can reach pre-cellular to intra-cellular resolutions and display pseudo-histological detail in the imaging of both neurons (**Fig. 6a**) and microvasculature (**Fig. 6b**). Comparatively, 2D toluidine blue histological staining of cord tissue, combined with optical microscopy imaging of thin slices, affords pre-cellular to intra-cellular structure visualizations that are superior in their (nanometric) spatial resolution, compared to sub-micron X-PCI-CT data (**Fig. 6c**). Histological views, though, are mono-directional and 2D, compared to 3D X-PCI-CTs, which enable, via virtual reslicing and 3D segmentation of data, morphological explorations of individual cells within deep neuronal populations in arbitrary planes and in 3D (**Fig. 6c**).

PFA-perfused & Tomato Lectin-labelled vessels within a 100 µm-thick slice of rat cord tissue were imaged with a confocal microscope at two different levels of magnification (**Fig. 6d**). This technology delivers 3D vascular representations that volumetrically outline endothelial-cell vessel-walls, rendering tube-like structures, especially well visible at the highest magnifications. Similar 3D vascular imaging was also achieved via X-PCI-CT, by locally scanning nervous tissues deep within extended PFA/Glu-fixed SC samples with sub-micron resolution setups, and then by segmenting out masks of hyper-intense voxels. This approach resulted in much more extended and dense vascular network representations (**Fig. 6d**).

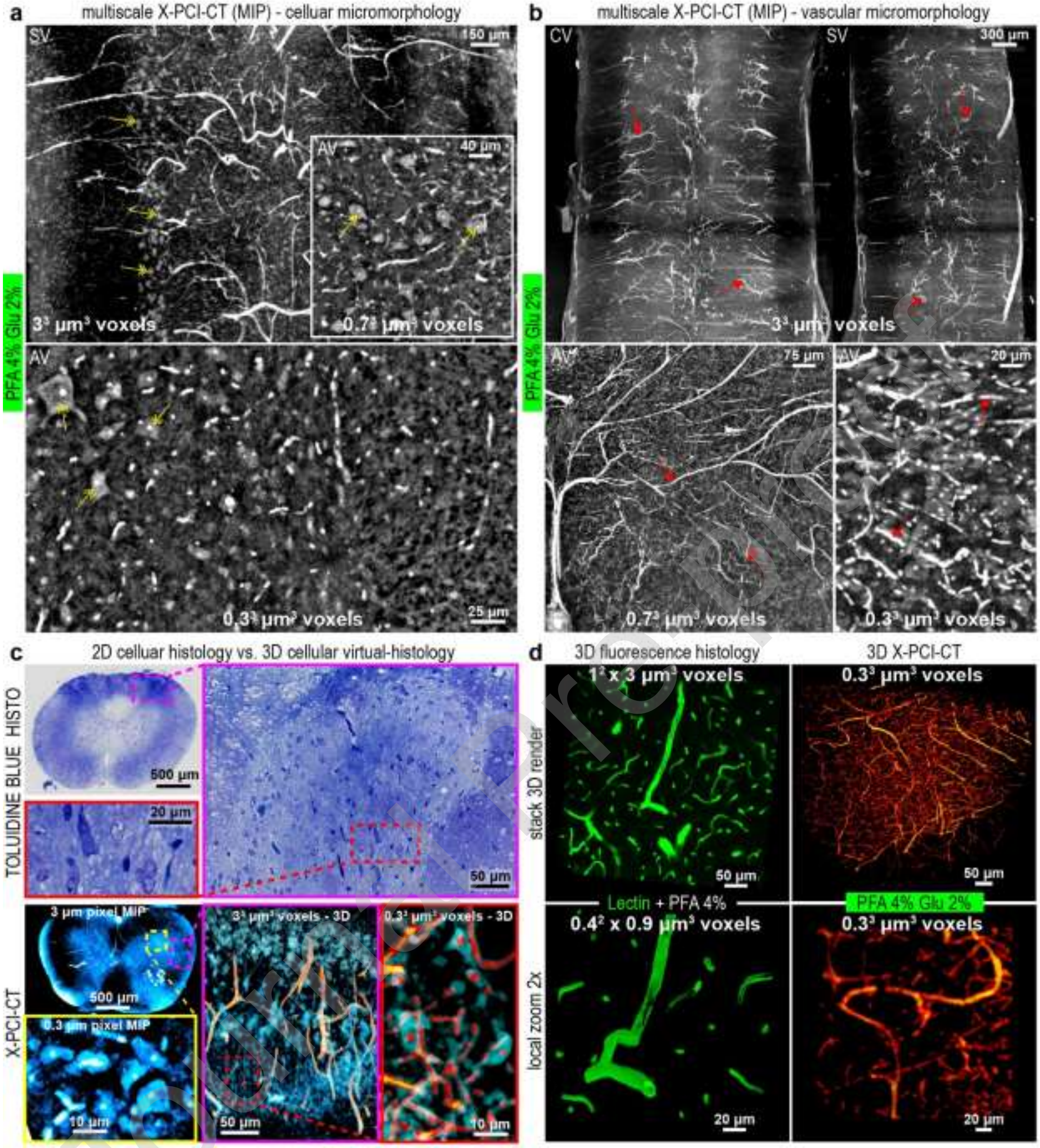

Figure 6. Multiscale 3D X-PCI-CT vs. 2D cellular histology and 3D vascular fluorescence-histology. (**a-b**) sagittal (SV), coronal (CV) and axial (AV) views of 3^3 to 0.3^3 µm^3 voxel multiscale 3D X-PCI-CT MIP maps of a dissected rat spinal cord fixed with PFA 4% + Glu 2%. MIPs computed with few (20-50) consecutive CT slices, in (**a**), visualize primarily cellular morphology. Adding more (50-200) consecutive CT slices to MIP maps, in (**b**), highlights extended vascular network morphology. Yellow arrows point to cellular microstructure at different scales, red arrows

to vascular microstructure at different scales. (**c-d**) state-of-the-art (**c**) 2D cellular imaging, i.e. 2D toluidine blue histology staining cellular structure (rendered in shades of blue), and (**d**) 3D vascular imaging, i.e. confocal fluorescence microscopy of Tomato-Lectin (Lectin) labelled & PFA-perfused vasculature (rendered green), vs. (**c**) recolored 2D MIP maps and 3D renderings of 3^3 to 0.3^3 µm^3 voxel multiscale X-PCI-CT data, emphasizing together cellular (rendered in shades of blue) & vascular anatomy (rendered red), and vs. (**d**) 3D renderings of 0.3^3 µm^3 voxel X-PCI-CT data, emphasizing only vascular anatomy (rendered red).

4. Discussion

Image contrast in multiscale X-PCI-CT of the spinal cord

Gray-levels and image contrast in propagation-based X-PCI-CT images can be easily interpreted, since phase-contrast arises due to differences in the electron density[23] within the imaged object, which in turn depends on the atomic number (Z) of the material[66]. Further, X-ray refraction effects make the technique very sensitive to object interfaces[67], and thus to internal object structures[68]. X-PCI-CT can be made quantitative by implementing specific image acquisition and post-processing procedures[69]. The phase-retrieval algorithm for single-distance propagation-based X-PCI-CT used here is fully-quantitative only in the limit of a monochromatic X-ray source and a homogenous object[58], but can still successfully deliver interpretable semi-quantitative measurements also of heterogeneous soft-tissue matter after irradiation with quasi-monochromatic to pink X-ray beams, as is our case here.

Within the native (unstained) soft-matter CNS tissues analyzed in this study, X-PCI-CT image soft-tissue contrast relates to small local differences in mass density, and can arise between different nervous tissue types (e.g. white vs. gray matter vs. cancerous tissue), due to high-Z material deposition (e.g. calcifications, blood) or due to internal anatomical structures with sharp edges (e.g. cells, vasculature)[26]. In the non-osmicated cord samples (**Fig. 1,3**), the observed image contrast is congruent with medullary local density differences and embedded structural features: denser gray-matter tissue yields higher gray-level values than white-matter, and denser somatic and nuclear structures (e.g. nucleoli) appear brighter than surrounding neuropil. The osmicated cords (**Fig. 1-2**), for their part, show how lipid cross-linkage, at the molecular level, by (strongly X-ray absorbing) $Os0_4$ metal leads, at the tissue level, to an (expected) enhancement of X-PCI-CT signal within stained myelinated white-matter, and thus to an inversion of white vs. gray matter image contrast.

As far as vascular structure imaging with X-PCI-CT goes, the sharp borders created by thick endothelial-cell vascular walls, as well as any deposits of dense iron-rich blood, concur to provide the highest image contrasts in unstained PFA- and PFA/Glu-fixed cords. Vascular gray-levels are followed by those of slightly hyper-dense cellular features, especially from motor neurons in spinal gray-matter horns. After osmium post-fixation, instead, white matter fiber and vascular structures contend the brightest image signals, and cellular features end up generating the lowest intra-medullary signals amongst these three structure types (**Fig. 2**).

When comparing different X-PCI-CT setups, gray vs. white matter contrast obtained using monochromatic X-rays (e.g. the data in **Fig. 1** & **Fig. 3c** with 3.0^3 and 0.3^3 μm^3 voxel sizes) was found generally higher than in X-PCI-CT data, obtained using pink X-ray beams (e.g. the data in **Fig. 3a** with 0.7^3 μm^3 voxel size). Structure contrast, instead, seems largely unaffected by the degree of mono-chromaticity (monochromatic vs. pink beams) of the X-rays used, and adequate microstructural characterization could be achieved using both beam types.

Sample preparation vs. image quality and microstructure detection

Overall, some evident image quality differences arise depending on the carried-out cord sample-preparation technique: osmium staining affords the most distinct delineations of neural structural boundaries and greatly enhances white vs. gray matter contrast (**Fig. 1, 3**). Especially well-visible after osmication is the fine structure of white matter fiber bundles, as well as individual nerve fibers intruding within the gray matter (**Fig. 2**). Vascular structure, instead, is better rendered within osmium-free medullas (**Fig. 1, 3**), and particularly after aldehyde fixation in combination (PFA 4%, Glu 2%). Compared to PFA 4% alone, the mixed aldehyde fixation protocol seems to lead to less image noise and more complete and detailed vascular trees (**Fig. 1**). OsO_4 impregnation, too, allows the visualization of vascular detail, mainly within gray-matter tissue. With this protocol, though, vessels compete against the bright osmium signal of myelin-rich areas, which hinders the visibility of vasculature within white-matter and leads to less complete vascular maps. Likewise, the quality of cellular structure visualizations appears as heterogeneous among differently prepared cords, with osmicated samples delivering the best portraits of cyto-architecture morphology, including some dendritic and axonal detail in addition to well-delineated hypo-dense cell-soma structure (**Fig. 2**, **Suppl. Fig. 1**). Glutaraldehyde fixation in combination with PFA, for its part, seems beneficial to staining-free cellular imaging, leading to somewhat better motor neuron soma demarcation within gray matter compared to gray-matter tissues fixed only with PFA, where local neuron soma structure appears more indistinct (**Fig. 1, 3**). Glutaraldehyde, and its superior protein cross-linking ability compared to PFA[41], is likely also responsible for the observed improved vascular and cellular visualizations in PFA/Glu-fixed samples, compared to just PFA-fixed ones. The Glu-component of this mixed-fixative protocol excels at preserving cellular and tissue microstructure[46], while the PFA-component makes the tissue penetration of the PFA/Glu combination quite quick. The benefits of a PFA/Glu fixation in combination are evident in the histological-resolution X-PCI-CT images obtained here (**Fig. 3**), showing well-defined (label-free & dense) cellular and intra-cellular structure alongside deep vasculature, all in 3D. Moreover, these imaging results are well recapitulated also in the collected cellular-level 2D toluidine blue-stained histological data (**Fig. 5**), which shows better-preserved nervous-tissue structures in the PFA/Glu case than in the PFA-only case.

While perfusion is considered the gold standard approach for CNS tissue fixation, *post-mortem* fixation by immersion, as performed here, is a viable alternative when specimens are small enough to allow effective fixative penetration, as is the case for the rodent SC samples. Fixation by immersion is also compatible with a possible future application of this imaging technology to human spine specimens *post-mortem*, a case for which perfusion would not constitute a viable option.

Still, no aldehyde fixative (or combination of aldehyde fixatives) can completely fix lipid components in CNS tissue, such as mixed protein/lipid structures within cell membranes: this result is, instead, normally achieved in CNS tissue sample-preparation protocols for TEM via post-fixation by osmium impregnation. The advantages of osmication, i.e. better cell-membrane preservation in addition to white-matter contrast enhancement, are well visible in the acquired cellular-level spinal nervous tissue X-PCI-CT data (**Fig. 2-3**) and histological data (**Fig. 5**), which capture the morphology of neuronal and axonal matter with the highest detail, owing to the superior degree of feature preservation and delineation afforded by the osmium staining. In conclusion, in this study osmium-stain cords proved to be the highest-quality samples for myelinated white-matter imaging and cellular sub-structure imaging (neuron perikarya, dendrites, axons), whereas PFA/Glu-fixed unstained cord samples proved to be the most reliable for multiscale vascular network imaging, including some local cellular and intra-cellular structure. Its independence from labels & contrast agents, and the relative protocol ease compared to osmium post-fixation, make the PFA/Glu the most readily-available and user-friendly of the sample-preparation techniques tested here.

3D quantification of CNS microstructure

The quantification of selected cellular and vascular parameters (**Fig. 4**), including sizes of cell-like structures and vascular thicknesses, demonstrates the possible use of X-PCI-CT data in the context of virtual-histological evaluations of 3D tissue volumes. In fact, based on the improved obtainable soft-tissue image contrast compared to absorption CTs, the collected spinal cord X-PCI-CT data could be masked to separate different 3D anatomical features within un-sectioned medullas. After segmentation, 3D masks could be analyzed with various 3D image analysis algorithms to extract quantitative distributions of meaningful morphological parameters.

For rodent spinal cord samples, such cellular-level analyses are limited (partially) by the duration of X-PCI-CT scans and synchrotron beam-time availability, and most of all by the size of collected CT volumes and by the computation durations of segmentation and analysis algorithms. Conversely, they are not limited by setup constraints, since the imaging FoV of the 3.0^3 μm^3 voxel setup is sufficient for the imaging of full soft-matter rodent cords, and the 0.7-0.3^3 μm^3 voxel setups can achieve image resolutions sufficient for cell imaging. Last, these X-PCI-CT-based quantifications are not hindered by sample-related constrains, since the fixed dissected SC samples are measured with no absolute prerequisite of either sample labeling, staining or sectioning.

The automatically-segmented masks of cellular structure presented here (**Fig. 4**), though, noticeably contain some unwanted microvasculature and other nervous tissue structure, which of course influence the resulting cellular-size distributions, at least to some degree. The manually-segmented masks used in vessel thickness measurements, for their part, seem to do a better job at extracting vascular features preferentially, this though at the price of a more arbitrary determination of threshold, and thus to a more biased quantification of extracted vascular network structure. It is to be expected, though, that the application of a more advanced segmentation methodology compared to the threshold-based one used in this study, may likely lead to more precise microstructure extractions and quantifications. A post-segmentation solution may, instead, involve filtering objects of different biological origin based on differing morphological parameters: rod-like vascular objects likely differ from spherical/oval cell-somas e.g. in terms of their surface/volume ratios. Any further design and implementation of segmentation methodology was deemed beyond the scope of this work, but will represent a necessary and important step in the future development of X-PCI-CT-based virtual-histological approaches for the automated 3D quantification of CNS tissue structure. Of interest to us, the performed data analysis seems sufficient to demonstrate that a quantification of deep 3D cellular-level features of the size of few microns is, at least in principle, feasible based on the multiscale datasets acquired here, for all sample preparation protocols.

X-PCI-CT vs. established volumetric and histological neuroimaging technologies

Post-mortem X-PCI-CT neuroimaging most closely relates to high-field PMMR neuroimaging, in that they both represent little-invasive soft-tissue-sensitive volumetric technologies. As highlighted in this work (**Fig. 5**), the foremost main advantage of X-PCI-CT with respect to PMMR is the higher achievable spatial resolution in measurements of CNS soft-tissue structure. Multiscale X-PCI-CT, in fact, enables intra-medullary micro-morphological visualizations of rodent neuron and intra-neuronal detail, which are beyond the possibility of current MRI technology. Second, X-PCI-CT seems better suited for vascular network imaging, owing to its high sensitivity to sharp internal sample borders and localized high-Z material dense deposits, as is the case for blood-filled (unperfused) multi-boundary vascular structures. Moreover, the generated density-based maps deliver complementary physical information with respect to PMMR. Last, the acquisition times for high-resolution synchrotron X-PCI-CT datasets are more moderate, in the order of tens of minutes, compared to PMMR datasets, which necessitate long measurement times in the order of tens of hours.

PMMR, for its part, achieves higher white vs. gray-matter contrast (**Fig. 5**), functional maps in addition to morphological ones, and a multiplicity of contrasts related to different physical parameters (e.g. relaxometry vs. diffusion vs. susceptibility maps, etc.). An advantage of PMMR specific to CNS imaging is an easier access to intra-skull and intra-spinal canal detail without the need for sample dissection, compared to X-PCI-CT measurements of CNS organs, for which the encasement within highly-absorbing and refracting bony structure represents a challenge[70]. More generally, PMMR has the undeniable further advantage of relatively compact one-room measurement setups, especially compared to synchrotron beamline X-PCI-CT setups, which exploit the brilliant X-rays of a dedicated large-scale scientific facility several hundreds of meters in diameter. More compact one-room X-ray light sources for X-PCI-CT applications[71] as well as simplified more-robust X-PCI-CT setups[72] are under development, with the objective to take the technique outside synchrotron facilities and thereby make the method more widely available. Overall though, since these two techniques provide, notably, complementary physical information, one based on tissue density and the other on nuclear spin systems, their side-by-side application may prove useful for future multimodal studies of CNS microanatomy.

PMMR aside, X-PCI-CT technology is naturally quite close to traditional 3D micro-CT neuroimaging, which also enables histology-like virtual 3D imaging. Compared to micro-CT, though, which relies heavily on contrast-enhancing impregnations and contrast-agent injections for brain and spinal cord (respectively) anatomical and vascular imaging, the work presented here shows that high intra-medullary vascular and cellular-feature contrast can be achieved in contrast-agent-free images by using the X-PCI-CT method. Further clear advantages of the X-PCI-CT measurements are the quickness and sub-micron resolution of the acquisitions, both unfeasible via traditional micro-CT in the absence of contrast agent.

The established possibility to image cellular and intra-cellular soft-tissue detail, including nervous tissue[73], allows referring to X-PCI-CT as a 3D virtual-histological technique[74]. Therefore, a direct comparison of X-PCI-CT data to established histological approaches for spinal cord structural imaging seemed warranted in this study (**Fig. 5-6**). Compared to virtual imaging with X-PCI-CT setups, traditional histological approaches to small-animal CNS micro-anatomical measurements involve the sectioning and eventual destruction of the CNS sample under analysis. Moreover, histological workups necessitate technically challenging manual procedures, and commonly lead to only mainly-2D visualizations, to anatomical distortions and subjective 3D reconstructions, to quantification-biasing artifacts of sample preparation, and to limits in the sample size due to constraints in the penetration of stains and dyes. On the contrary, X-PCI-CT allows for non-destructive virtual spatially-aligned 3D visualizations of CNS tissue in arbitrary planes of evaluation, and for staining- and label-free dense quantifications of microstructure with fewer (at least theoretical) limits in sample size, and less-biased (since dense and label-free) morphological representations. Admittedly, though, image artifacts due to *post-mortem* nervous tissue fixation[41], such as artifactual dark neurons, differential neuropil retraction and shrinkage, mucocytes or other white-matter artifacts, are present also in CNS X-PCI-CT datasets, since they depend on pre-imaging sample-preparation procedures related to fixation. Moreover, a relatively complex dissection of the cord before sample fixation was necessary also to collect the X-PCI-CT data in this study. Last, the osmium-stained visualizations presented here suffer from the same dye/label tissue-penetration issues typical of other histological imaging approaches, such as TEM or immuno-histology, or traditional absorption-based micro-CT. Homogenous osmium-penetration within non-dissected rodent spinal cords, for example, might prove a challenging step prior to X-PCI-CT scanning, so that, depending on the sample, X-PCI-CT may also have to face sample-size limitations due to sample-preparation issues, when osmium impregnation is involved.

Perhaps, the most interesting results from spinal cord X-PCI-CT, both here and in previous works, relate to vascular imaging. Here, vascular networks were extracted from CT datasets based on threshold segmentations, with vascular gray-levels relating to the intrinsic density of blood-filled vascular structure and to the edges created by thick endothelial-cell vascular wall linings. This vessel detection method is simple, completely independent of labels or contrast agents, and delivers unbiased dense and quantitative 3D representations of extended vascular networks at relatively high spatial resolution. Compared to this approach, fluorescence microscopy of vascular networks (**Fig. 6**), which relies on indirect label-based measurements for vascular structure sensitivity, suffers from sparse labelling issues and labelling-related bias[75]. Moreover, the spatial extension of (Lectin)-labelled vascular networks is limited by the initial choice of tissue slice thickness, and this vascular imaging approach becomes increasingly more complicated with increasingly larger sample sizes. The sample size allowed for similar X-PCI-CT-based acquisitions of 3D contrast-agent-free vasculature, instead, is limited only by the number of contiguous datasets acquired during imaging (and thus by the overall measurement times) and by the increasingly large datasets, which will arise for increasingly large samples, leading to a rise in post-processing times (e.g. data reconstruction and analysis duration) and in the needed virtual storage-space. Last, while fluorescence-microscopy-based vascular measurements can currently still achieve the highest spatial resolutions, X-PCI-CT and its 3D renderings of capillary-level microstructure were shown here to not trail too far behind in terms of resolving power, and thus in terms of measurable level of micro-vascular detail.

5. Conclusions

Non-invasive 3D visualizations of full-organ CNS micro-vascularization and of neuronal cellular microstructure are fundamental in the preclinical study of vascular and neurodegenerative diseases, and yet they are still difficult to obtain with current cutting edge imaging technology. In this study, carried out *post-mortem* on extracted animal-model spinal cord samples, we demonstrate that multiscale X-PCI-CT permits a unique volumetric histology-like analysis & quantification of intra-medullary neuronal and vascular microstructure. The technique, in fact, can detect the micromorphology of deep single cells and single micro-vessels within extended soft-matter samples, after little sample preparation and in the absence of any neuronal labeling or staining. Interestingly, the crucial role of an adapted and robust nervous tissue fixation protocol for the development of better-designed and more specific neuroimaging approaches was (once more) made evident by the analysis of the effect on image quantity of different aldehyde fixation and post-fixation protocols performed as part of this study. A comparative qualitative evaluation of the imaging results for differently-prepared SC samples led to valuable insight on the suitability of the tested sample preparation procedures for differently-oriented CNS microstructural studies: for example, a PFA/Glu fixation in combination was deemed most effective for spinal cord micro-vascular studies. PFA/Glu with the addition of osmium post-fixation, instead, was deemed ideal for studies on myelination and white-matter fiber structure. Last, these results confirm that the application of synchrotron radiation X-PCI-CT for non-invasive volumetric *post-mortem* CNS tissue imaging, i.e. the employment of a technique, which can achieve the cellular resolution of histological approaches combined with the 3D soft-tissue sensitivity of PMMR, may arguably be able to provide new opportunities for neuroimaging. Several advantages of an X-PCI-CT-based approach to neuroimaging, compared to established PMMR, traditional micro-CT, histology and fluorescence microscopy approaches, was discussed in detail. For all these reasons, X-PCI-CT seems fit to potentially improve current micrometric neuro-anatomical investigations of the CNS in animal models, and impact both neuroanatomical and neuropathological research.

CRediT Author Statement

Giacomo E. Barbone: Investigation, Methodology, Software, Validation, Formal Analysis, Data Curation, Visualization, Writing - Original Draft

Alberto Bravin: Conceptualization, Methodology, Resources, Writing - Review & Editing, Supervision

Alberto Mittone: Investigation, Methodology, Software, Validation, Data Curation, Writing - Review & Editing

Markus J. Kraiger: Investigation, Validation, Data Curation

Martin Hrabě de Angelis: Resources, Supervision, Funding acquisition

Mario Bossi: Investigation, Data Curation

Elisa Ballarini: Investigation, Validation, Writing - Review & Editing

Virginia Rodriguez-Menendez: Investigation, Validation, Writing - Review & Editing

Cecilia Ceresa: Investigation, Data Curation

Guido Cavaletti: Conceptualization, Resources, Writing - Review & Editing, Supervision, Funding acquisition

Paola Coan: Conceptualization, Methodology, Writing - Review & Editing, Supervision, Funding acquisition, Project administration

Acknowledgements:

This work was supported by the Deutsche Forschungsgemeinschaft (Cluster of Excellence) - Munich Center for Advanced Photonics [EXE158], by the International Max Plank Research School of Advanced Photon Science (IMPRS-APS), by a European COST Action [CA16122], and by the German Federal Ministry of Education and Research [Infrafrontier Grant 01KX1012 to M.H.d.A.]. Authors acknowledge the Paul Scherrer Institut, Villigen, Switzerland for provision of synchrotron radiation beamtime at TOMCAT beamline of the SLS. Authors acknowledge the European Synchrotron Radiation Facility for provision of beam time and laboratory facilities, and for electronic, computing, and software assistance; moreover, authors thank Dr. Herwig Requardt for technical support. Finally, the authors thank the German Mouse Clinic of the Helmholtz Zentrum Munchen for allowing the use of their 9.4T MRI scanner.

References:

1. Annese, J. *et al.* Postmortem examination of patient H.M.'s brain based on histological sectioning and digital 3D reconstruction. *Nat. Commun.* **5**, 3122 (2014).

2. Ding, S.-L. *et al.* Comprehensive cellular-resolution atlas of the adult human brain. *J. Comp. Neurol.* **524**, 3127–3481 (2016).

3. Schmitz, C. & Hof, P. R. Design-based stereology in neuroscience. *Neuroscience* **130**, 813–831 (2005).

4. Duval, T. *et al.* Axons morphometry in the human spinal cord. *Neuroimage* **185**, 119–128 (2019).

5. Sear, R. P. *et al.* Life at the mesoscale : the self-organised cytoplasm and nucleoplasm. *BMC Physiol.* **8**, 4–9 (2015).

6. Loureiro, J. R. *et al.* In-vivo quantitative structural imaging of the human midbrain and the superior colliculus at 9.4T. *Neuroimage* **177**, 117–128 (2018).

7. Calabrese, E. *et al.* Postmortem diffusion MRI of the entire human spinal cord at microscopic resolution. *NeuroImage Clin.* **18**, 963–971 (2018).

8. Sengupta, S. *et al.* High resolution anatomical and quantitative MRI of the entire human occipital lobe ex vivo at 9.4T. *Neuroimage* **168**, 162–171 (2018).

9. Harrison, M. *et al.* Vertebral landmarks for the identification of spinal cord segments in the mouse. *Neuroimage* **68**, 22–29 (2013).

10. Arthurs, O. J. *et al.* Diagnostic accuracy and limitations of post-mortem MRI for neurological abnormalities in fetuses and children. *Clin. Radiol.* **70**, 872–880 (2015).

11. Pallebage-Gamarallage, M. *et al.* Dissecting the pathobiology of altered MRI signal in amyotrophic lateral sclerosis: A post mortem whole brain sampling strategy for the integration of ultra-high-field MRI and quantitative neuropathology. *BMC Neurosci.* **19**, 11 (2018).

12. Beaujoin, J. *et al.* Post-mortem inference of the human hippocampal connectivity and

microstructure using ultra-high field diffusion MRI at 11.7 T. *Brain Struct. Funct.* **223**, 2157–2179 (2018).

13. Plantinga, B. R. *et al.* Ultra-High Field MRI Post Mortem Structural Connectivity of the Human Subthalamic Nucleus, Substantia Nigra, and Globus Pallidus. *Front. Neuroanat.* **10**, 66 (2016).

14. Schmierer, K. *et al.* Quantifying multiple sclerosis pathology in post mortem spinal cord using MRI. *Neuroimage* **182**, 251–258 (2018).

15. de Bournonville, S., Vangrunderbeeck, S. & Kerckhofs, G. Contrast-Enhanced MicroCT for Virtual 3D Anatomical Pathology of Biological Tissues: A Literature Review. *Contrast Media Mol. Imaging* **2019**, 8617406 (2019).

16. Senter-Zapata, M. *et al.* The Role of Micro-CT in 3D Histology Imaging. *Pathobiology* **83**, 140–147 (2016).

17. Chen, K.-C., Arad, A., Song, Z.-M. & Croaker, D. High-definition neural visualization of rodent brain using micro-CT scanning and non-local-means processing. *BMC Med. Imaging* **18**, 38 (2018).

18. Saito, S., Mori, Y., Yoshioka, Y. & Murase, K. High-resolution ex vivo imaging in mouse spinal cord using micro-CT with 11.7T-MRI and myelin staining validation. *Neurosci. Res.* **73**, 337–340 (2012).

19. Masís, J. *et al.* A micro-CT-based method for quantitative brain lesion characterization and electrode localization. *Sci. Rep.* **8**, 5184 (2018).

20. Kirschner, S. *et al.* Imaging of Orthotopic Glioblastoma Xenografts in Mice Using a Clinical CT Scanner: Comparison with Micro-CT and Histology. *PLoS One* **11**, e0165994 (2016).

21. Unnikrishnan, G. *et al.* A 3-D Rat Brain Model for Blast-Wave Exposure: Effects of Brain Vasculature and Material Properties. *Ann. Biomed. Eng.* **47**, 2033–2044 (2019).

22. Bravin, A., Coan, P. & Suortti, P. X-ray phase-contrast imaging: from pre-clinical applications towards clinics. *Phys. Med. Biol.* **58**, R1–R35 (2013).

23. Cloetens, P., Barrett, R., Baruchel, J., Guigay, J.-P. & Schlenker, M. Phase objects in synchrotron radiation hard x-ray imaging. *J. Phys. D. Appl. Phys.* **29**, 133–146 (1996).

24. Beltran, M. a *et al.* Interface-specific x-ray phase retrieval tomography of complex biological organs. *Phys. Med. Biol.* **56**, 7353–7369 (2011).

25. Schulz, G. *et al.* Multimodal imaging of human cerebellum - merging X-ray phase microtomography, magnetic resonance microscopy and histology. *Sci. Rep.* **2**, 826 (2012).

26. Barbone, G. E. *et al.* Micro-imaging of Brain Cancer Radiation Therapy Using Phase-contrast Computed Tomography. *Int. J. Radiat. Oncol. Biol. Phys.* **101**, 965–984 (2018).

27. Khimchenko, A. *et al.* Hard X-Ray Nanoholotomography: Large-Scale, Label-Free, 3D Neuroimaging beyond Optical Limit. *Adv. Sci.* **5**, 1700694 (2018).

28. Haghayegh Jahromi, N. *et al.* A Novel Cervical Spinal Cord Window Preparation Allows for Two-Photon Imaging of T-Cell Interactions with the Cervical Spinal Cord Microvasculature during Experimental Autoimmune Encephalomyelitis. *Front. Immunol.* **8**, 406 (2017).

29. Soderblom, C. *et al.* 3D Imaging of Axons in Transparent Spinal Cords from Rodents and Nonhuman Primates. *eNeuro* **2**, e.0001-15.2015 (2015).

30. Massimi, L. *et al.* Characterization of mouse spinal cord vascular network by means of synchrotron radiation X-ray phase contrast tomography. *Phys. Medica* **32**, 1779–1784 (2016).

31. Pinzer, B. R. *et al.* Imaging brain amyloid deposition using grating-based differential phase contrast tomography. *Neuroimage* **61**, 1336–1346 (2012).

32. Massimi, L. *et al.* Exploring Alzheimer’s disease mouse brain through X-ray phase contrast tomography: From the cell to the organ. *Neuroimage* **184**, 490–495 (2019).

33. Cao, Y. *et al.* Visualization of mouse spinal cord intramedullary arteries using phase- and attenuation-contrast tomographic imaging. *J. Synchrotron Radiat.* **23**, 966–974 (2016).

34. Fratini, M. *et al.* Simultaneous submicrometric 3D imaging of the micro-vascular network and the

neuronal system in a mouse spinal cord. *Sci. Rep.* **5**, 8514 (2015).

35. Hu, J. *et al.* Nondestructive imaging of the internal micro-structure of vessels and nerve fibers in rat spinal cord using phase-contrast synchrotron radiation microtomography. *J. Synchrotron Radiat.* **24**, 482–489 (2017).

36. Bartels, M., Krenkel, M., Cloetens, P., Möbius, W. & Salditt, T. Myelinated mouse nerves studied by X-ray phase contrast zoom tomography. *J. Struct. Biol.* **192**, 561–568 (2015).

37. Hu, J., Cao, Y., Wu, T., Li, D. & Lu, H. 3D angioarchitecture changes after spinal cord injury in rats using synchrotron radiation phase-contrast tomography. *Spinal Cord* **53**, 585–590 (2015).

38. Miao, P. *et al.* Synchrotron Radiation X-Ray Phase-Contrast Tomography Visualizes Microvasculature Changes in Mice Brains after Ischemic Injury. *Neural Plast.* **2016**, 3258494 (2016).

39. Cao, Y. *et al.* Three Dimensional Quantification of Microarchitecture and Vessel Regeneration by Synchrotron Radiation Microcomputed Tomography in a Rat Model of Spinal Cord Injury. *J. Neurotrauma* **34**, 1187–1199 (2017).

40. Cedola, A. *et al.* X-Ray Phase Contrast Tomography Reveals Early Vascular Alterations and Neuronal Loss in a Multiple Sclerosis Model. *Sci. Rep.* **7**, 5890 (2017).

41. Fix, A. S. & Garman, R. H. Practical Aspects of Neuropathology: A Technical Guide for Working with the Nervous System. *Toxicol. Pathol.* **28**, 122–131 (2000).

42. Stefanutti, E. *et al.* Assessment of the effects of different sample perfusion procedures on phase-contrast tomographic images of mouse spinal cord. *JINST* **13**, C03027 (2018).

43. Saccomano, M. *et al.* Synchrotron inline phase contrast µCT enables detailed virtual histology of embedded soft-tissue samples with and without staining. *J. Synchrotron Radiat.* **25**, 1153–1161 (2018).

44. Töpperwien, M., Markus, A., Alves, F. & Salditt, T. Contrast enhancement for visualizing neuronal cytoarchitecture by propagation-based x-ray phase-contrast tomography. *Neuroimage* **199**, 70–80

(2019).

45. Strotton, M. C. *et al.* Optimising complementary soft tissue synchrotron X-ray microtomography for reversibly-stained central nervous system samples. *Sci. Rep.* **8**, 12017 (2018).

46. Park, C.-H., Kim, H.-W., Rhyu, I. J. & Uhm, C.-S. How to Get Well-Preserved Samples for Transmission Electron Microscopy. *Appl. Microsc.* **46**, 188–192 (2016).

47. Chiorazzi, A. *et al.* Experimental epothilone B neurotoxicity: Results of in vitro and in vivo studies. *Neurobiol. Dis.* **35**, 270–277 (2009).

48. Snigirev, A., Snigireva, I., Kohn, V., Kuznetsov, S. & Schelokov, I. On the possibilities of x- ray phase contrast microimaging by coherent high- energy synchrotron radiation. *Rev. Sci. Instrum.* **66**, 5486–5492 (1995).

49. Stampanoni, M. *et al.* TOMCAT: A beamline for TOmographic Microscopy and Coherent rAdiology experimenTs. *AIP Conf. Proc.* **879**, 848–851 (2007).

50. Mader, K. *et al.* High-throughput full-automatic synchrotron-based tomographic microscopy. *J. Synchrotron Radiat.* **18**, 117–124 (2011).

51. Mittone, A. *et al.* Characterization of a sCMOS-based high-resolution imaging system. *J. Synchrotron Radiat.* **24**, 1226–1236 (2017).

52. Optique Peter. (2019). Available at: http://www.optiquepeter.com. (Accessed: 10th April 2020)

53. Suortti, P. *et al.* Fixed-exit monochromator for computed tomography with synchrotron radiation at energies 18-90keV. *J. Synchrotron Radiat.* **7**, 340–347 (2000).

54. Weitkamp, T., Haas, D., Wegrzynek, D. & Rack, A. ANKAphase: software for single-distance phase retrieval from inline X-ray phase-contrast radiographs. *J. Synchrotron Radiat.* **18**, 617–629 (2011).

55. Mittone, A. *et al.* Multiscale pink beam microCT imaging at the ESRF-ID17 biomedical beamline. *J. Synchrotron Radiat.* **Accepted**, (2020).

56. Mirone, A., Brun, E., Gouillart, E., Tafforeau, P. & Kieffer, J. The PyHST2 hybrid distributed code for high speed tomographic reconstruction with iterative reconstruction and a priori knowledge capabilities. *Nucl. Instruments Methods Phys. Res. Sect. B* **324**, 41–48 (2014).

57. Marone, F., Studer, A., Billich, H., Sala, L. & Stampanoni, M. Towards on-the-fly data post-processing for real-time tomographic imaging at TOMCAT. *Adv. Struct. Chem. Imaging* **3**, 1 (2017).

58. Paganin, D., Mayo, S. C., Gureyev, T. E., Miller, P. R. & Wilkins, S. W. Simultaneous phase and amplitude extraction from a single defocused image of a homogeneous object. *J. Microsc.* **206**, 33–40 (2002).

59. Schneider, C. A., Rasband, W. S. & Eliceiri, K. W. NIH Image to ImageJ: 25 years of image analysis. *Nat. Methods* **9**, 671–675 (2012).

60. Lyckegaard, A., Johnson, G. & Tafforeau, P. Correction of ring artifacts in X-ray tomographic images. *Int. J. Tomogr. Stat.* **18**, 1–9 (2011).

61. Kapur, J. N., Sahoo, P. K. & Wong, A. K. C. A new method for gray-level picture thresholding using the entropy of the histogram. *Comput. Vision, Graph. Image Process.* **29**, 273–285 (1985).

62. Bolte, S. & Cordelières, F. P. A guided tour into subcellular colocalization analysis in light microscopy. *J. Microsc.* **224**, 213–232 (2006).

63. Hildebrand, T. & Rüegsegger, P. A new method for the model-independent assessment of thickness in three-dimensional images. *J. Microsc.* **185**, 67–75 (1997).

64. Robertson, R. T. *et al.* Use of labeled tomato lectin for imaging vasculature structures. *Histochem. Cell Biol.* **143**, 225–234 (2015).

65. Flood, D. G. & Coleman, P. D. Neuron numbers and sizes in aging brain: Comparisons of human, monkey, and rodent data. *Neurobiol. Aging* **9**, 453–463 (1988).

66. Zachariasen, W. *Theory of X-ray diffraction in crystals*. (J. Wiley & Sons Inc, 1945).

67. Cloetens, P. *et al.* Holotomography: Quantitative phase tomography with micrometer resolution using hard synchrotron radiation x rays. *Appl. Phys. Lett.* **75**, 2912–2914 (1999).

68. Betz, O. *et al.* Imaging applications of synchrotron X-ray phase-contrast microtomography in biological morphology and biomaterials science. I. General aspects of the technique and its advantages in the analysis of millimetre-sized arthropod structure. *J. Microsc.* **227**, 51–71 (2007).

69. Nugent, K. A., Gureyev, T. E., Cookson, D. F., Paganin, D. & Barnea, Z. Quantitative Phase Imaging Using Hard X Rays. *Phys. Rev. Lett.* **77**, 2961–2964 (1996).

70. Zamir, A. *et al.* X-ray phase contrast tomography; proof of principle for post-mortem imaging. *Br. J. Radiol.* **89**, 20150565 (2016).

71. Eggl, E. *et al.* X-ray phase-contrast tomography with a compact laser-driven synchrotron source. *PNAS* **112**, 5567–5572 (2015).

72. Zamir, A. *et al.* Recent advances in edge illumination X-ray phase-contrast tomography. *J. Med. Imaging* **4**, 040901 (2017).

73. Töpperwien, M. *et al.* Three-dimensional mouse brain cytoarchitecture revealed by laboratory-based x-ray phase-contrast tomography. *Sci. Rep.* **7**, (2017).

74. Töpperwien, M., Krenkel, M., Quade, F. & Salditt, T. Laboratory-based x-ray phase-contrast tomography enables 3D virtual histology. in *Proceedings of the SPIE* **9964**, 99640I (2016).

75. Farhoodi, R., Lansdell, B. J. & Kording, K. P. Quantifying How Staining Methods Bias Measurements of Neuron Morphologies. *Front. Neuroinform.* **13**, 36 (2019).